

1 **Decoding the Dynamics of Climate Change Impact: Temporal Patterns of Surface**
2 **Warming and Melting on the Nivlisen Ice Shelf, Dronning Maud Land, East**
3 **Antarctica**

4 Geetha Priya M ^{a,*}, Raghavendra K R ^a, Mahesh B ^a, Rakshita C ^a, Dhanush S ^a, Sivaranjani S ^a, Deva Jefflin A R ^a,
5 Krishna Venkatesh ^a, Narendra Kumar M ^a, Alvarinho J. Luis ^b

6 ^aCentre for Incubation Innovation Research and Consultancy (CIIRC), Jyothy Institute of Technology, Bengaluru 560082, Karnataka, India

7 ^bNational Centre for Polar and Ocean Research, Ministry of Earth Sciences, Vasco-da-Gama, Goa 403 804, India

8 *Corresponding author: geetha.sri82@gmail.com

9 **Abstract.** The dynamics of surface melting in Antarctica play a crucial role in understanding glacier and ice sheet
10 behavior and monitoring climate change in polar regions. This study focuses on analyzing various aspects of the
11 Nivlisen ice shelf in East Antarctica, including melt ponds, supraglacial lakes (SGLs), seasonal surface melt extent,
12 and surface ice flow velocity. Data from Landsat and Sentinel-1 for the austral summers between 2000 and 2023 were
13 used for spatial and temporal analysis. During November and December from 2000 to 2014, the overall area of melt
14 ponds and SGLs on the ice shelf remained relatively low, measuring approximately one square kilometer. However,
15 from 2015 to 2023, there was a consistent increase in surface melting, resulting in the formation of more melt ponds
16 and SGLs. Significant SGL depths were observed in 2016, 2017, 2019, and 2020, while the years 2008, 2016, and
17 2020 exhibited the highest volumes and progressive growth in SGL area. To understand the impact of surface melting
18 on ice shelf dynamics, the relationship between seasonal surface melt extent and surface ice flow velocity was
19 examined. The findings were validated through ground truth data collected from a melt pond in central Dronning
20 Maud Land during the austral summer of 2022-2023, along with model-based results. The integration of Unmanned
21 Aerial Vehicle (UAV) survey and the installation of Pressure Sensor Assembly (PSA) effectively addressed the
22 validation challenge posed by the unavailability of cloud-free data. The observed increase in melt pond depth and
23 volume could significantly affect the stability of the ice shelf. Persistent surface melting conditions are likely to
24 amplify the formation of melt ponds and SGLs, resulting in accelerated ice flow and potential ice shelf destabilization.
25 Continuous monitoring of Antarctic ice shelves is vital to assess the ongoing impact of climate change accurately.

26
27 **Keywords:** Surface Melt, Melt Pond, Ice flow velocity, UAV, Pressure sensor, Antarctica, Landsat, Sentinel-1

28

29

30

31

32

33

34 **1 Introduction**

35 Ice shelves play a crucial role in regulating the ice flow from Antarctica to the ocean,
36 making them significant features in the Polar Regions (Bell et al. 2017; Dell et al. 2020). However,
37 the increasing surface melting on Antarctic ice shelves due to climate change has led to a greater
38 loss of ice (Bell et al. 2017; Dell et al. 2020). Rising temperatures and changing precipitation
39 patterns are responsible for the escalated ice melting and loss (Arthur, C.R. Stokes, et al. 2020).
40 Efficient subglacial drainage mechanisms are essential for maintaining uninterrupted ice flow and
41 the calving process of ice shelves, making their preservation a major concern (Tuckett et al. 2021;
42 Sneed and Hamilton 2007; Stevens et al. 2015). Recent measurements indicate a rise in surface
43 melting across the Antarctic continent, further highlighting the impact of environmental changes
44 (Husman et al. 2022; Luis et al. 2022; Saunderson et al. 2022; Valerio et al. 2022). These changes
45 have far-reaching consequences, affecting the meridional temperature gradient, sea level rise,
46 atmospheric conditions, ocean biogeochemical dynamics, and other factors (Rintoul 2018).

47 Understanding the consequences of melting on ice shelves is crucial for comprehending
48 Antarctica's contribution to rising sea levels (Geetha Priya et al. 2022; Jakobs et al. 2020;
49 Baumhoer et al. 2018; Ghiz et al. 2021). Surface albedo, weather patterns like heat waves and
50 extreme events, and other factors significantly influence the amount of surface melt, which exhibits
51 significant year-to-year variability (Mortimer et al. 2016; Hall et al. 2009; Saunderson et al. 2022).
52 Even minor changes in ice shelves can have significant global effects on sea level rise and climate
53 patterns (Husman et al. 2022). Prolonged and intense surface melting can give rise to melt ponds
54 and supraglacial lakes (SGL), contributing to ice shelf instability (Liang et al. 2021; Colosio et al.
55 2021; König and Oppelt 2020). Meltwater accumulates in depressions, leading to the formation of
56 SGLs (Dell et al. 2022; Moussavi et al. 2020). While these lakes are transient, they vary in size,
57 depth, and spatial distribution. Some SGLs can extend for several kilometers and reach depths of
58 several meters. Analyzing variations in the volume and area of circular or linear surface water
59 bodies helps us better understand meltwater dynamics (Dell et al. 2020). SGLs typically undergo
60 cycles of formation and drainage, with most lakes reabsorbing or emptying during the austral
61 summer (Hawes et al. 2011). However, some SGLs drain through crevasses, moulins, melt
62 channels, or other drainage features, potentially impacting the underlying ice dynamics
63 (Leppäranta et al. 2020; Dell et al. 2020; Sneed and Hamilton 2007; Liu et al. 2022)

64 The presence of melt ponds and SGLs reduces the surface reflectivity (albedo) of glaciers,
65 resulting in increased solar energy absorption and enhanced surface melting (Lombardi et al. 2019;
66 Jakobs et al. 2021). This process further destabilizes ice shelves by warming the surrounding ice
67 column (Furfaro et al. 2014; Fricker et al. 2021). SGL characteristics, including size, depth,
68 distribution, and atmospheric variables like temperature and radiation, play a complex role in the
69 relationship between SGL development, surface albedo, and ice shelf dynamics (Arthur, C. Stokes,
70 et al. 2020; Buzzard et al. 2018). The presence and behavior of SGLs have significant implications
71 for ice shelf stability and their impact on inland ice flow (Arthur, C. Stokes, et al. 2020; Arthur et
72 al. 2022; Liu et al. 2022).

73 The formation of SGLs in Antarctica can occur through various mechanisms, such as the
74 accumulation of meltwater on ice sheets or glaciers, leading to the development of ponds or lakes.
75 The lower albedo of these water bodies increases solar radiation absorption, accelerating surface
76 melting (Arthur, C. Stokes, et al. 2020; Luis et al. 2022; Jakobs et al. 2020; Halas et al. 2023; Hall
77 et al. 2009; Lampkin and Karmoskay 2009; Alley 2017). This localized increase in surface melting
78 contributes to greater meltwater production and expansion of lakes (Mahagaonkar, A et al. 2023;
79 Dirscherl et al. 2020). Additionally, glacial lakes facilitate the flow of meltwater to the ice shelf's
80 base, causing accelerated melting and compromising the shelf's structural integrity, potentially
81 leading to collapse (Izeboud and Lhermitte 2023). Understanding the interaction between SGLs,
82 surface albedo, and ice shelf dynamics is vital for comprehending ice shelf behavior and stability
83 under changing environmental conditions (Gardner and Sharp 2010).

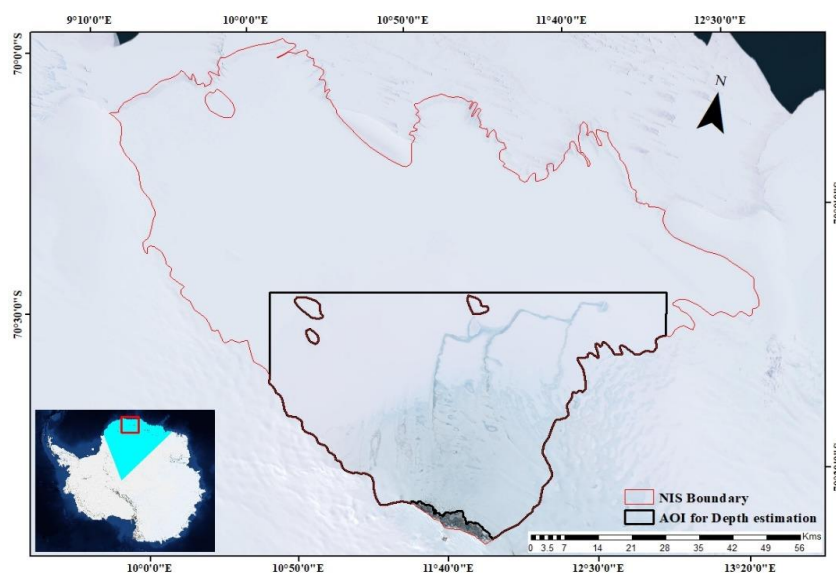
84 In this study, we utilize microwave Synthetic Aperture Radar (SAR) and optical data to
85 estimate various parameters of the Nivlisen Ice Shelf (NIS) on the east coast of Antarctica,
86 including surface melt extent, SGL characteristics (depth, area, volume), and surface ice flow
87 velocity. While optical data can underestimate the true extent of meltwater due to limited
88 availability of cloud-free imagery, field measurements using pressure sensors validate pond depth
89 estimates obtained from UAV multispectral data. The findings of this research provide valuable
90 insights into the vulnerability of the NIS to climate change, contributing to our understanding of
91 surface melting, melt ponds and SGLs, and the increasing meltwater, with implications for future
92 sea level rise predictions (Pina and Vieira 2022; Qiao et al. 2023). The objective of this study is to
93 conduct a comprehensive technical analysis of the dynamics of the Nivlisen Ice Shelf (NIS) in East
94 Antarctica. Using satellite data from the Landsat and Sentinel-1 datasets, the analysis will be

95 conducted at both spatial and temporal scales (Alimasi et al. 2020; Kaushik et al. 2022). The
96 primary goals are to estimate surface melt extent, determine various parameters related to SGLs
97 (area, length, volume, depth), analyze ice shelf velocity, and assess the influence of surface melt
98 on seasonal ice velocity patterns. Field measurements utilizing pressure sensors to monitor
99 meltwater levels are employed for empirical verification of the results.

100 **2 Study Area**

101 Antarctica, renowned for its vast ice sheets, encompasses approximately 98% of the landmass in
102 the Antarctic region. Within East Antarctica, a significant territory known as Dronning Maud Land
103 sprawls across more than 2.7 million square kilometers. This expansive region boasts a coastline
104 stretching approximately 2,000 kilometers, characterized by immense ice shelves. The degree of
105 surface ice loss serves as a critical determinant in assessing the extent of melting on these ice
106 shelves (Arthur, C. Stokes, et al. 2020; Vaňková et al. 2021; Bell et al. 2018; Ghiz et al. 2021;
107 Husman et al. 2022; Alley 2017). The selection of Nivlisen Ice Shelf (NIS) for this study stems
108 from the recent surge in melt ponds and surface-generated lakes (SGLs) observed within the ice
109 shelf region. Moreover, NIS experiences significant melting throughout the austral summer,
110 resulting in the formation of SGLs. These phenomena render the ice shelf increasingly susceptible
111 to hydrofracturing (Cook and Vaughan 2010; Jakobs et al. 2020; Aoki et al. 2017; Baumhoer et al.
112 2018; Kingslake et al. 2017; Liang et al. 2021; Trusel et al. 2022), making it a pivotal area for
113 investigating the processes and causes leading to ice loss on the Antarctic ice shelf (Trusel et al.
114 2012). Figure 1 illustrates the expansive nature of NIS, covering an area of approximately 7,600
115 square kilometers and extending around 80 kilometers north to south and 130 kilometers east to
116 west into the Lazarev Sea (Dell et al. 2020). Situated within the center of Dronning Maud Land
117 (cDML) at coordinates 70.3S and 11.3E, NIS possesses ice thickness ranging from 150 to 700 m.
118 The Vigrid and Lazarev ice shelves flank NIS, while the Potsdam Glacier feeds it from the
119 southeast, contributing an average ice thickness of 1,000 m. In the southeastern corner of the ice
120 shelf, the exposed ice moves at an average speed of 80 m per year due to katabatic winds. The
121 southern part of NIS encompasses the Schirmacheroasen, an ice-free region with lakes, ponds, and
122 a maximum elevation of 250 m above sea level (Lindbäck et al. 2019). During the summer months,
123 surface melting occurs, resulting in the creation of melt ponds and SGLs across various regions of
124 NIS, including its north, west, and southern sectors. Since 2016, there has been a notable evolution
125 in meltwater ponding attributed to rising temperatures. As a consequence, NIS is experiencing

126 accelerated melting, making it a strategically significant location for investigating the dynamics
127 and factors influencing ice loss on the Antarctic ice shelf (Alley et al. 2018).



128
129 **Fig. 1.** Study area on East Antarctica consisting of Nivlisen Ice Shelf, central Dronning Maud
130 Land located at 70.3 °S,11.3°E with a 2000 km coastline encompassing large ice shelves with the
131 coordinate reference system “WGS84 Antarctic polar stereographic.”

132 3 Data

133 For assessing seasonal variations in melt ponds and supraglacial lakes (SGLs), satellite-based
134 multispectral datasets were used. Landsat-7, Landsat-8, and Landsat-9 satellites provided data
135 during the austral summer with minimal cloud cover. Landsat-7, launched in 1999, has eight
136 spectral bands and 15-30 m resolution. Landsat-8, launched in 2013, offers 11 spectral bands and
137 15-100 m resolution. Landsat-9, launched in 2021, shares the same capabilities. Synthetic Aperture
138 Radar (SAR) data was obtained from the Alaska Satellite Facility. Sentinel-1 SAR data, part of
139 the Copernicus Earth monitoring program, was used for surface melt and velocity estimations.
140 Sentinel-1A and Sentinel-1B, launched in 2014 and 2016, respectively, provide high-resolution
141 images with a revisit period of 6 days. The data utilized include Sentinel-1 Level-1 Interferometric
142 Wide (IW) swath Ground Range Detected (GRD) and Single Look Complex (SLC) products.
143 These data sources contribute to understanding surface melt and velocity over the Nivlisen ice
144 shelf (NIS). **Supplementary Table S1 and S2 provide the specific datasets used.**

145 4 Methodology

146 Figure 2 depicts the comprehensive process flow utilized to capture the seasonal patterns
 147 and variations of surface melt, specifically in the form of melt ponds and Supraglacial Lakes
 148 (SGLs) over the NIS region. The methodology incorporates an InSAR (Interferometric Synthetic
 149 Aperture Radar) based displacement estimation technique.

150 4.1 Melt Pond Depth Model

151 The satellite data collected are initially in Digital Number (DN) format, which needs to be
 152 converted to Top of Atmosphere (TOA) reflectance. Equations 1 and 2 are employed for the visible
 153 bands (red and blue) to achieve this conversion. The TOA reflectance is corrected for the sun's
 154 angle, taking into account the sun's zenith and elevation angles. Bedrock masking is applied to the
 155 TOA blue and red bands.

$$156 \quad \rho' = M_{Rf} Q_{Cal} + A_{Rf} \quad (1)$$

$$157 \quad \rho = \frac{\rho'}{\cos(\theta_{SZ})} = \frac{\rho'}{\cos(\theta_{SE})} \quad (2)$$

158 Where Q_{Cal} is the visible band in DN format, ρ' is TOA reflectance without correction for the sun's
 159 angle, M_{Rf} is a multiply rescaling factor (band specific), A_{Rf} is an additive rescaling factor (band
 160 specific), ρ is TOA reflectance with correction for the sun's angle, θ_{SZ} is the sun's zenith angle, and
 161 θ_{SE} is the sun's elevation angle

162 The modified Normalized Difference Water Index for icy locations (NDWI_ICE) is then
 163 calculated using the blue and red visible bands to map the melt ponds and SGLs over the ice shelf
 164 (Equation 3). NDWI_ICE accentuates the spectral differences between unfrozen water and
 165 relatively arid snow/ice surfaces. A threshold value of 0.25 is used to identify the melt ponds and
 166 SGLs, which is adjusted by 0.01 based on the amount of water visible in the false-color composite.
 167 The areas of the melt ponds and SGLs are calculated using the vectorized raster (Arthur, C. Stokes,
 168 et al. 2020; Dell et al. 2020).

$$169 \quad NDWI_{ICE} = \frac{(BLUE_{Ref} - RED_{Ref})}{(BLUE_{Ref} + RED_{Ref})} \quad (3)$$

170 Where, $BLUE_{Ref}$ is the blue visible band reflectance and RED_{Ref} is the red visible band
 171 reflectance.

172 To estimate the depth (L_d) of the melt ponds and SGLs, a multispectral data-based Melt
 173 Pond Depth (MPD) model (Equation 4) is utilized (Philpot 1989; Sneed and Hamilton 2007; Pope
 174 et al. 2016; Arthur et al. 2022; Geetha Priya et al. 2022). The model is based on the radiative
 175 transfer principle, simulating the interaction of light with different components such as the water
 176 column, underlying aquatic bottom, and surrounding environment. The depth calculation relies on
 177 the rate of light attenuation in water, determined by the absorption and scattering properties of the
 178 water. Additionally, knowledge of the lake bottom's albedo, which affects the reflected light, is
 179 essential for accurate depth estimation. The proportion of dissolved and suspended materials
 180 impacts the reflectance of optically deep water, potentially affecting the depth estimation.

$$181 \quad L_d = \frac{[\ln(L_{br} - R_\infty) - \ln(R_{Ld} - R_\infty)]}{\alpha} \quad (4)$$

182 Where, L_{br} is peripherals reflectance of the lake, R_∞ is the reflectance of optically deep water, R_{Ld}
 183 is the reflectance of the water body, α is the attenuation constant. The L_{br} was calculated for each
 184 melt pond/SGL in every scene by averaging two pixels buffer. The mean variation between using
 185 $R_\infty = 0$ (i.e., reflectance from open ocean water) and using R_∞ values obtained from the lakes in
 186 the scenarios is less than 10%. As a result, the R_∞ value was considered to be nil for all scenes

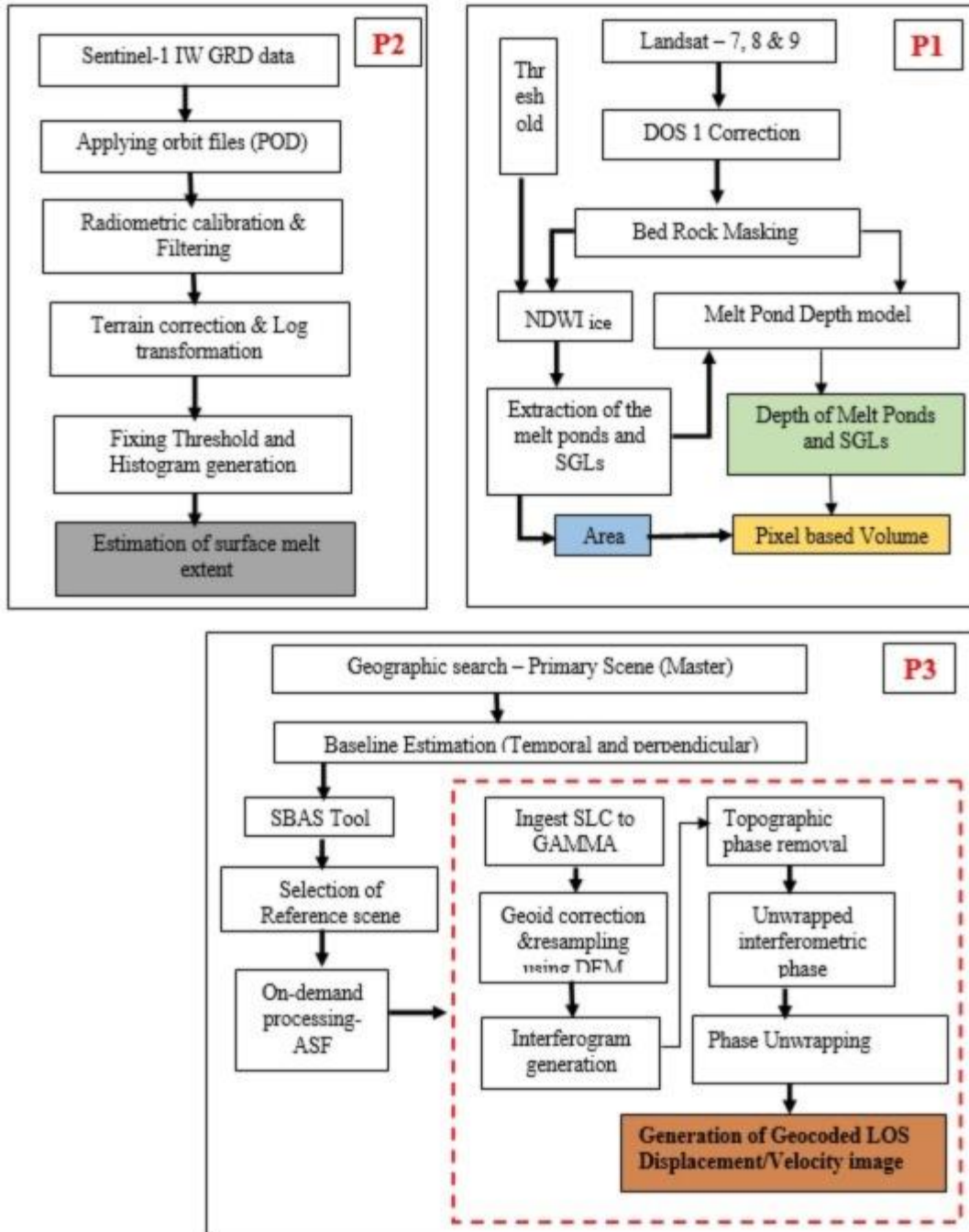
187 4.2 Estimation of Surface melt extent

188 The surface melt extent over NIS involves processing Sentinel-1 Synthetic Aperture Radar
 189 (SAR) data using the SNAP algorithm. The data is calibrated to obtain backscatter values (σ^0) (Zhu
 190 et al. 2023), followed by speckle noise reduction and correction for geometric distortions and
 191 topographic variations. The calibrated data is then transformed into decibels, and the extent of
 192 surface melt is determined by thresholding the resulting histogram. This process, outlined in Jewell
 193 Lund et al., 2022, generates a binary image that delineates the area of interest (Lund et al. 2022).

194 4.3 Surface ice velocity

195 The Alaska Satellite Facility (ASF) provides access to On Demand services ([https://hyp3-
 196 docs.asf.alaska.edu/using/vertex/](https://hyp3-docs.asf.alaska.edu/using/vertex/)) for generating SAR interferometry products from Sentinel-1
 197 data. By selecting reference and secondary scenes through geographic search in Alaska Vertex,
 198 interferograms are constructed. The Baseline tool ensures coherent phase measurements by
 199 identifying data with reasonable perpendicular baseline values for InSAR processing. SBAS
 200 utilizes a large number of interferograms with short baselines and high temporal resolution. Pre-

201 and post-processing steps involve data import, geoid correction, burst estimation, mosaicking,
 202 unwrapping, and phase unwrapping using SNAPHU. The final output includes geocoded velocity
 203 information (Sivalingam et al. 2022).



204

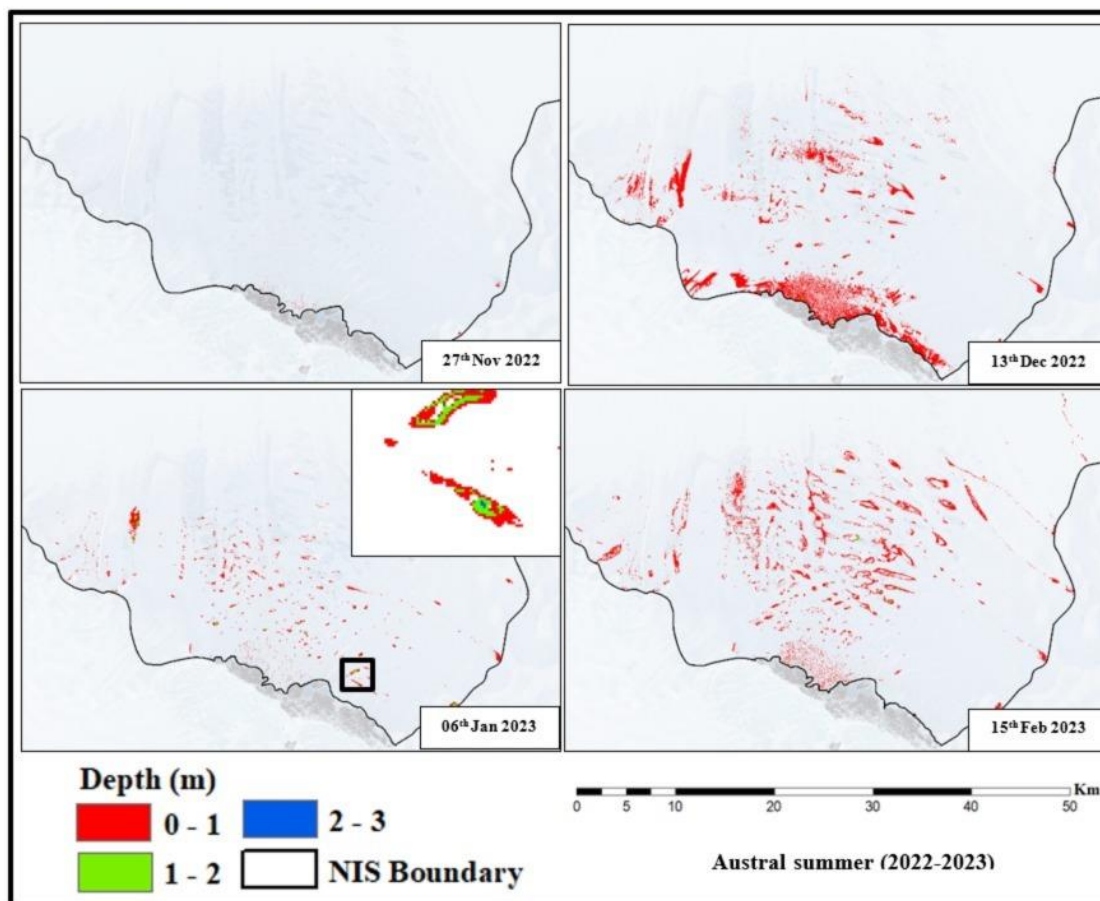
205 **Fig. 2.** Process flow – Estimation of surface melt extent (P1), depth of melt ponds and
 206 Supraglacial lakes using melt pond depth model, area and volume (P2), and ice flow velocity
 207 using (P3).

208 **5 Results and Discussion**

209 **5.1 Dynamics of melt ponds and SGLs**

210 A pixel-based approach was used to estimate the depth of melt ponds and SGLs on the ice
211 shelf, following the methodology in section 4.1 (Fig 2., P2). By analyzing individual pixel values
212 and incorporating the MPD model's depth profile, more accurate volume estimation was achieved,
213 overcoming limitations of conventional methods and ensuring reliability of the results. The study
214 encompassed austral summers from 2000 to 2023, focusing on the peak melt period. The depth
215 estimates are presented in supplementary Figures S1-S8 and Figure 3, highlighting the trend over
216 the years. The analysis revealed a relatively low total area of melt ponds and SGLs (<1 km²) in
217 November and December from 2000 to 2014. However, a significant increase in meltwater volume
218 was observed in January and February, representing the peak meltwater volume of the season (Hall
219 et al. 2009; Orr et al. 2022; Vaňková et al. 2021). A consistent pattern of melting and increased
220 formation of melt ponds and SGLs was observed during the NDJF period from 2015 to 2023
221 (Figure 3). These findings provide insights into the seasonal variability of meltwater accumulation
222 and the timing and magnitude of peak meltwater volume in the study area. The distribution of melt
223 ponds and SGLs showed clustering, with a higher concentration observed in the southern
224 grounding zone. Conversely, the central part of the ice shelf exhibited minimal melt ponds and
225 SGLs due to lower surface melt rates. The results were analyzed in conjunction with weather data
226 obtained from the Meteostat database for the study area, specifically weather station No. 89512.
227 The temperature trend from 2000 to 2023 is depicted in Figure 3.

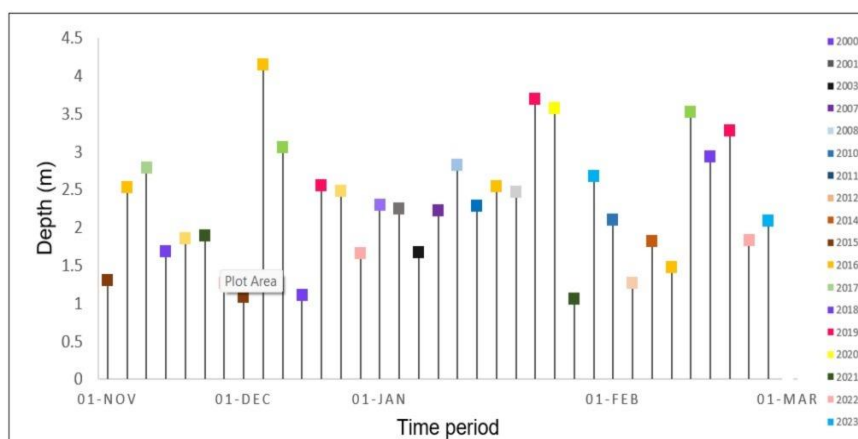
228



229

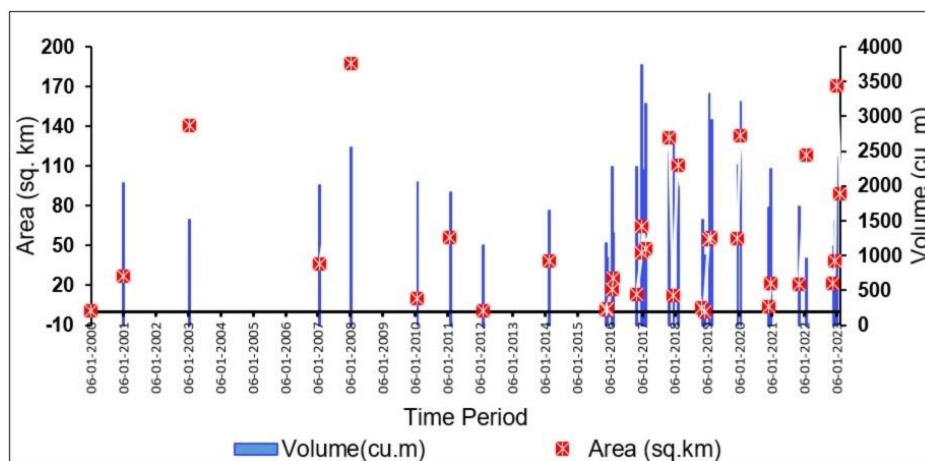
230

Fig. 3. Model-based melt pond depth for the austral summer of 2022–2023.



231

Fig. 4. Maximum depth during austral summers of 2000-2023.



232

233

Fig. 5. Area and volume during austral summers of 2000-2023

234

235 On January 6, 2000, the melt ponds and Subglacial Lakes (SGLs) in Antarctica reached a
 236 maximum depth of 2.3 m, with a volume of 2,070.52 m³ and an area of 1.203 km². The following
 237 year, on January 1, 2001, the maximum depth was 2.25 m, with an area of 27.081 km² and a
 238 volume of 2,033.63 m³. Despite the average temperature being -1.1°C on January 14, 2003, the
 239 maximum depth of the melt ponds and SGLs was 1.68 m, covering an area of 140.83 km² and a
 240 volume of 1,516.46 m³. The maximum depth and volume decreased in 2003 compared to the
 241 previous years, while the area of the melt pond increased. On January 18, 2007, the highest depth
 242 and volume were 2.23 m and 2,007.38 m³, respectively, covering an area of 36.18 km². These
 243 values increased compared to 2003, possibly due to higher average and maximum temperatures.
 244 On January 26, 2010, the maximum depth and volume were 2.29 m and 2,050.51 m³, respectively,
 245 with an area of 10.26 km². The peak values for depth, area, and volume occurred on January 5,
 246 2008, measuring approximately 2.83 m, 187.18 km², and 2,547.56 m³, respectively, between 2000
 247 and 2010. On February 5, 2011, the depth and volume decreased, while the area increased to 55.83
 248 km², indicating significant growth compared to January 2010. Similarly, on February 2, 2012, the
 249 depth, area, and volume significantly decreased to 1.28 m, 1.05 km², and 1,148.79 m³, respectively,
 250 possibly due to environmental factors. On February 14, 2014, with lower temperatures compared
 251 to 2012, the maximum depth and volume were 1.83 m and 1,643.41 m³, respectively, covering an
 area of 38.73 km².

252

253

254

Throughout the austral summers spanning from 2015 to 2020, there were variations in the
 maximum depth, area, and volume of melt ponds and Subglacial Lakes (SGLs) in Antarctica.
 Noteworthy findings include the highest recorded maximum depth and volume of 2.54 m and

255 2,278.52 m³, respectively, on January 26, 2016. The maximum area of 24.99 km² was observed on
256 February 2, 2016. The austral summer of 2016 to 2017 witnessed the peak depth (4.15 m) and
257 volume (3,736.76 m³) on December 27, 2016, attributed to the highest average and maximum
258 temperatures. Similarly, in the austral summer of 2017 to 2018, the estimated maximum depth and
259 volume of SGLs were 3.06 m and 2,750.92 m³, respectively, associated with elevated temperature
260 records. In the following years, 2018 to 2020, higher values of maximum depth and volume were
261 recorded, indicating fluctuating temperatures during the peak melt season.

262 During the austral summers from 2020 to 2021, the maximum depth, area, and volume of
263 SGLs increased significantly on December 22, 2020, attributed to higher temperature records. For
264 the austral summers of 2021 to 2022, larger values were recorded on November 7, 2021, but the
265 volume decreased by January 26, 2022. Drainage through fissures and canals likely caused the
266 reduction. During the austral summers of 2022 to 2023, higher values were observed on January
267 6, 2023, but decreased by February 15, 2023, due to temperature drop and drainage mechanism.

268 During the Antarctic summer, surface lakes are common in inland ice shelf areas, while
269 central parts have fewer Supraglacial Lakes (SGLs). Fluctuations in lake area result in varying
270 meltwater volume throughout the season. Higher melt rates lead to increased surface runoff,
271 establishing a linear relationship between SGL area and volume. Since 2000, SGL depth, area, and
272 volume have increased. The years 2016, 2017, 2019, and 2020 exhibit maximum SGL depth. 2008,
273 2016, and 2020 show maximum volume with a gradual area increase. The highest area occurred
274 in January 2008 and 2023, with an increase from January 2022 followed by a mid-February
275 decline. These findings align with IPCC and Bell et al.'s predictions of increasing surface
276 meltwater coverage and volume on Antarctic ice shelves due to rising temperatures.

277 **5.2 Seasonal surface melt and surface ice flow velocity variations of the NIS: Limitations** 278 **and Focus on austral summers 2019-2023**

279 The objective of this study is to estimate the seasonal surface melt and surface ice flow
280 velocity of the NIS in East Antarctica, focusing specifically on the austral summer period from
281 November to February. The analysis is limited to the austral summers of 2019-2023 due to data
282 constraints. The MEaSURES Program of NASA provides ice motion data from 1996 to 2016 on
283 annual scale, while Sentinel-1 data is available from 2014 onwards. However, suitable InSAR pairs
284 for ice surface displacement/velocity analysis were not found for the austral summers from 2014

285 to 2019. Similarly, suitable InSAR pairs from ERS, ALOS PALSAR, and RADARSAT satellites
286 were limited or unavailable for the period from 2000 to 2014 in the study area.

287 **5.3 Seasonal surface melt extent**

288 The surface melt extent (SME) map, estimated for austral summers from 2019 to 2023,
289 shows melt detected in the northwest and southern parts of the shelf, while the center remains dry.
290 Figure 6 depict temperature, surface melt extent, and precipitation patterns, contributing to the
291 understanding of surface melting in the study region.

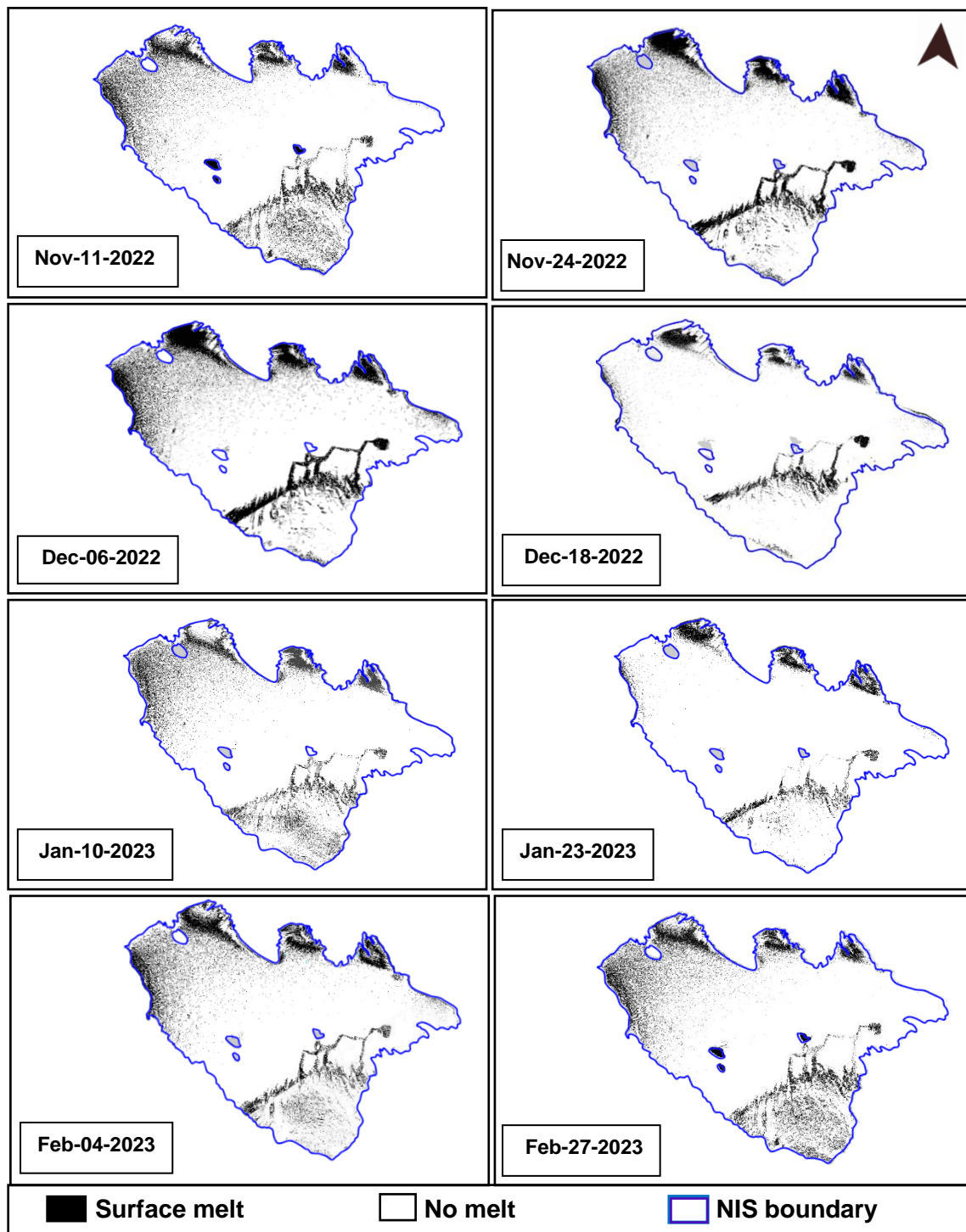
292 In November 2019, a significant surge in surface melting occurred with an average melt area
293 of 1,531 km². The mean temperature during this period fluctuated between -7.9°C and -1.2°C. In
294 December 2019, the average melt area expanded to 2,102 km², coinciding with a mean temperature
295 range of -3.9°C to 2.9°C. On December 15, 2019, the highest recorded mean temperature of 1.6°C
296 was observed. In January 2020, the average extent of surface melt reached 2,202 km², showing a
297 slight increase compared to December. The monthly average temperature ranged from -5°C to
298 2.7°C. February 2020 experienced a substantial escalation in the average surface melt area, totaling
299 3,086 km², accompanied by an average temperature range of -6.8°C to 0.6°C. This increase in
300 melting may be influenced by the albedo effect, which amplifies the melting process.

301 In November 2020, the estimated surface melt area reached approximately 1,519 km²,
302 similar to the values observed in November 2019. The mean temperature during that period ranged
303 from -13.1°C to -0.3°C, with recorded precipitation of 4.1mm. December 2020 showed a decrease
304 in surface melt area, with an estimated average of 1,239 km², coinciding with a rise in mean
305 temperature from -4.8°C to 1.4°C. However, factors such as high freezing winds and wind chill
306 variations could have contributed to the reduction in surface melt area. January 2021 marked the
307 peak melt season, with an expanded surface melt area of 2,474 km², accompanied by an average
308 temperature rise from -6.1°C to 3.8°C. In February 2021, the average surface melt area decreased
309 to 1,947 km², accounting for two-thirds of the extent observed in February 2020, with a mean
310 temperature range of -8.4°C to -1.4°C.

311 In November 2021, the surface melting in the region increased, with an average surface melt
312 area of approximately 1,618 km². The mean temperature during this period ranged from -12.3°C
313 to -1.5°C. This represented an increase of around 100 km² compared to the surface melt observed
314 in November 2019 and 2020. December 2021 experienced a significant rise in the melt area,
315 reaching approximately 2,392 km², primarily due to higher temperatures ranging from -4.5°C to

316 0.9°C. In January 2022, despite being the peak melt season, the average extent of surface melt
317 decreased to 2,177 km², possibly due to recorded precipitation in late December 2021 and January
318 2022. February 2022 witnessed a further reduction in the average surface melt area to 1,702 km²,
319 correlated with a significant decrease in the average temperature. Overall, the austral summer of
320 2021-2022 demonstrated increased surface melting in December compared to other months.

321 In November 2022, there was a significant increase in surface melting, with an average
322 surface melt area of 3,187 km². This marked a substantial rise compared to previous Novembers.
323 The mean temperature during this period ranged from -10°C to -1.9°C. However, in December
324 2022, there was a reduction in surface melting despite an increase in temperature and recorded
325 precipitation of 0.3 mm. The average surface melt area was around 3,083 km². In January 2023,
326 the average extent of surface melt decreased to 2,735 km², possibly due to the chilling effect of
327 freezing katabatic winds. February 2023 witnessed an increase in surface melt, with an average
328 surface melt of 3,725 km², similar to patterns observed in February 2020, potentially influenced
329 by the albedo effect. The analysis of surface melt during the austral summers of 2019-2020 to
330 2022-2023 highlights variations in melt extent influenced by temperature, precipitation, and
331 external factors.

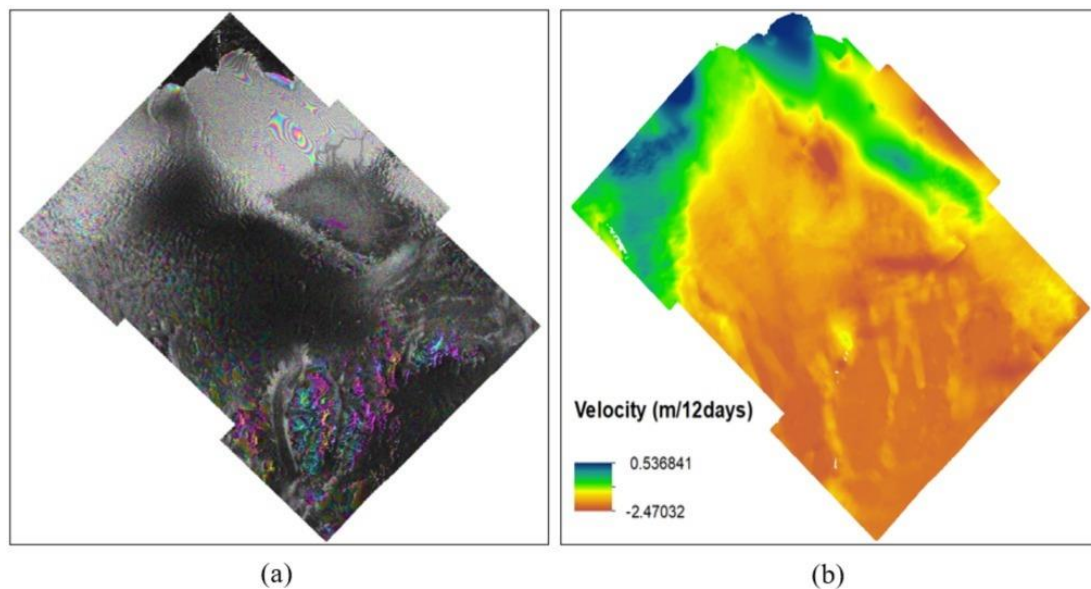


332 **Fig. 6.** The surface melt extent (SME) map over NIS for the austral summer 2022-2023

333

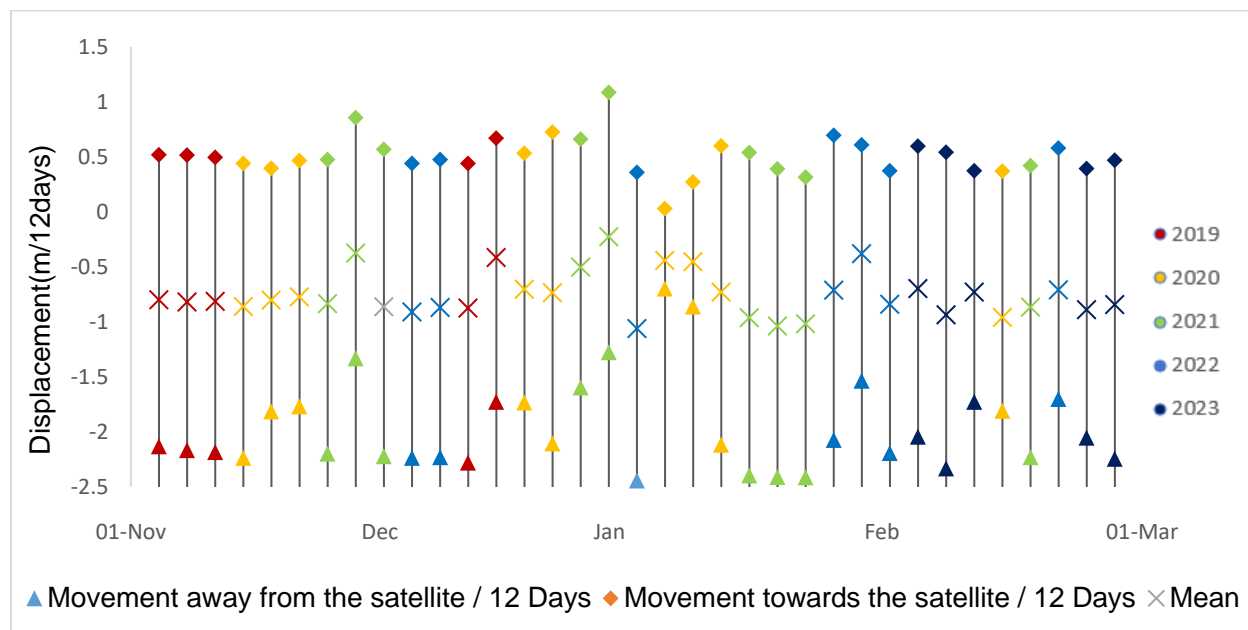
334 **5.4 Seasonal surface ice flow velocity**

335 Unwrapped interferograms generate displacement maps, quantifying ground movement in
336 meters and direction relative to the satellite's radar line-of-sight. Measurements were collected
337 during the austral summers of 2019-2023. Figure 18 displays the unwrapped phase and velocity
338 map for January 10 and January 22, 2023, as an illustrative example.



339

340 **Fig. 7.** (a) The unwrapped phase and (b) surface ice flow velocity map obtained during January
341 10, 2023 (master) and January 22, 2023 (slave) over Dronning Maud Land (Negative values
342 indicate movement in the direction away from the satellite along the radar line-of-sight, while
343 positive values indicate movement towards the satellite along the radar line-of-sight)



344

345 **Fig. 8.** The velocity obtained for 12-day time period during the months of austral summers
 346 considered for the study.

347 The ice velocity data for the austral summer of 2019-2020 indicates a gradual increase over
 348 time. In mid-November 2019, the velocity measured 2.13 m/12 days, which slightly increased to
 349 2.18 m/12 days by the end of the month. This upward trend is supported by an average velocity of
 350 0.8 m/12 days during that period. However, a contrasting pattern emerges in December 2019, as
 351 the velocity declines from 2.28 m/12 days to 1.72 m/12 days. The mean velocity at the end of
 352 December 2019 is recorded at 0.44 m/12 days, deviating from the previous upward trend.

353 Moving into January 2020, the velocity starts at 0.69 m/12 days but undergoes a significant
 354 increase to 2.11 m/12 days by the end of the month. This surge in velocity indicates a notable
 355 acceleration likely related to the peak melt season. The early part of February to mid-February
 356 2020 marks the peak velocity period, with a mean velocity of 0.96 m/12 days. However, there is a
 357 subsequent decrease in the velocity values, dropping from 2.11 m/12 days to 1.81 m/12 days.
 358 Comparing the different time periods, it is interesting to note that the velocity observed in
 359 December 2019 surpasses that of November 2019, January, and February 2020.

360 In the austral summer of 2020-2021, the ice velocity shows some variations. In November,
 361 the velocity decreases from 2.23 m/12 days to 1.81 m/12 days. Moving into December, the velocity
 362 reaches 1.73 m/12 days. In January, the velocity increases to 2.41 m/12 days, suggesting a potential

363 correlation between velocity and the peak melt season. However, in February, the velocity
364 decreases, making the relationship less clear.

365 For the austral summer of 2021-2022, there is a significant decline in velocity observed. In
366 early November 2021, the velocity measures 2.20 m/12 days, but by the end of November, it
367 decreases to 1.33 m/12 days. However, in early December, there is a temporary recovery with a
368 velocity of 2.22 m/12 days. From mid-December to the end of December 2021, the velocity
369 decreases once again. The velocity values fluctuate from mid-January to the end of February 2022,
370 but the mean velocity shows a decreasing trend.

371 In the austral summer of 2022-2023, the velocity remains relatively consistent at 2.23 m/12
372 days from mid-November to early December 2022. However, there is a decrease in the mean
373 velocity. From mid-December to the end of December 2022, the velocity shows a noticeable
374 decrease. The velocity values continue to fluctuate until the end of February 2023, with a slight
375 increase in velocity but a decrease in the mean velocity.

376 These observations highlight the variations in ice velocity during different austral summer
377 periods. The analysis reveals that surface melt and velocity in NIS are interconnected. Higher
378 maximum and mean velocity values consistently occur in January during austral summers from
379 2019 to 2023, indicating significant melting. December exhibits greater velocity fluctuations,
380 suggesting instability and the onset of melting. Understanding the connection between velocity
381 and surface melting is crucial for ice shelf dynamics and stability. These findings enhance our
382 understanding of the relationship between surface melt, velocity, and the future of NIS.

383 **5.5 Seasonal surface Melt and surface ice flow velocity patterns during the austral** 384 **summer 2019-2023**

385 Velocity and surface melt are important parameters for understanding ice sheet dynamics
386 and climate change impacts. Examining their relationship provides valuable insights into the
387 interplay between ice dynamics and surface processes in Polar Regions. Analyzing data and trends
388 can reveal correlations and deepen our understanding of the region's dynamics during austral
389 summers.

390 In November 2019, the surface melt area increased to 1,531 km², and the velocity rose from
391 2.13 m/12 days to 2.18 m/12 days, indicating a positive correlation between surface melt and
392 velocity. However, in December 2019, while the surface melt area expanded to 2,102 km², the

393 velocity declined to 1.72 m/12 days, suggesting a possible decoupling. January 2020 showed a
394 slight increase in both the surface melt area (2,202 km²) and velocity (2.11 m/12 days), partially
395 restoring the positive relationship. February 2020 exhibited significant increases with a surface
396 melt area of 3,086 km² and a peak velocity of 2.11 m/12 days. Overall, surface melt and velocity
397 are positively correlated, indicating a feedback mechanism between them.

398 In November, the velocity decreases from 2.23 m/12 days to 1.81 m/12 days, while the
399 surface melt area remains similar at 1,519 km², suggesting an inverse correlation. In December,
400 both the surface melt area and velocity fall to around 1,239 km² and 1.73 m/12 days, respectively,
401 indicating a potential positive association. In January, an increase in velocity to 2.41 m/12 days
402 leads to a significant rise in surface melt (2,474 km²) during the peak melt season. However, in
403 February, both surface melt (1,947 km²) and velocity (2.23 m/12 days) decrease, showing a weaker
404 link.

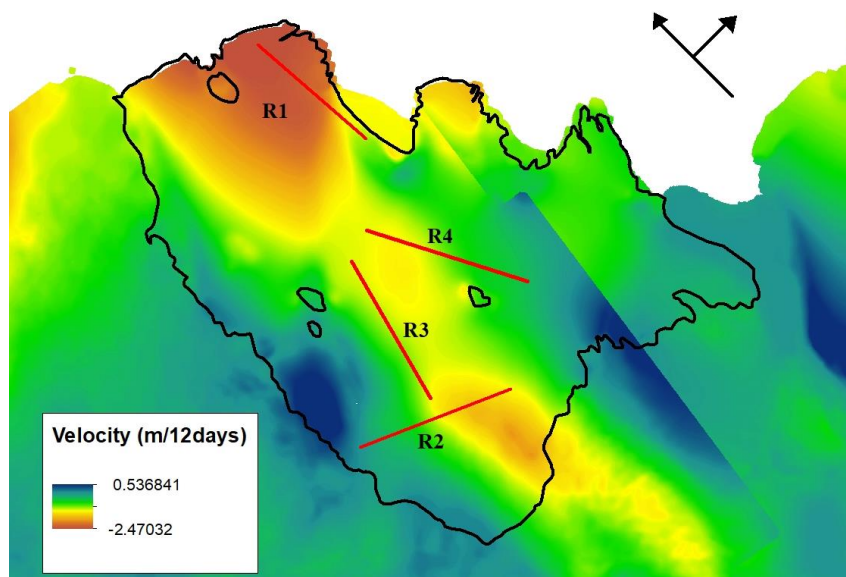
405 In November 2021, the surface melt area increases to 1,618 km² while the velocity
406 decreases to 1.33 m/day, suggesting an inverse correlation. By December 2021, the surface melt
407 expands to around 2,392 km², accompanied by a slight velocity increase to 2.22 m/day. In January
408 2022, the surface melt area decreases to 2,177 km², possibly influenced by precipitation and
409 fluctuating velocity. In February 2022, the surface melt area further declines to 1,702 km², and
410 velocity remains erratic. The analysis indicates a complex interaction between surface melt and
411 velocity during the 2021-2022 austral summer, influenced by temperature, precipitation, and other
412 factors.

413 In November 2022, the velocity remains constant at 2.23 m/12 days while the
414 surface melt area rises to 3,187 km², indicating a potential positive correlation. However, in
415 December 2022, despite a decrease in surface melt area to 3,083 km², the velocity also decreases,
416 suggesting a weakening association. In January 2023, the surface melt area further decreases to
417 2,735 km², while the velocity fluctuates, highlighting the complex relationship. A subsequent
418 increase in both surface melt area (3,725 km²) and velocity in February 2023 may signify the
419 restoration of a positive link. The analysis predicts a dynamic interaction between surface melt and
420 velocity during the 2022-2023 austral summer, influenced by temperature, precipitation, and wind
421 patterns.

422 The surface melt-displacement relationship varied across different austral summer periods.
423 While some periods showed strong correlations (e.g., November 2019 and February 2023), others
424 exhibited weak or no correlation (e.g., December 2019 and January 2021). Fluctuations observed
425 may be influenced by factors like wind patterns, precipitation, and local conditions. To understand
426 this relationship, further research considering these variables is needed

427 **5.6 Dynamics of ice flow in melt and non-melt regions of NIS: Velocity Insights from** 428 **Profiles R1-R4**

429 Early in the melt season, small surface lakes form at Schirmacheroasen in relatively flat
430 areas near the grounding line of the NIS. Analyzing the velocity patterns in the melt and non-melt
431 regions of the NIS provides valuable information. Four linear profiles (R1, R2, R3, and R4) were
432 selected, spanning the NIS with a length of 30 km each (Figure 21). R1 and R2 represent the melt
433 regions of the ice shelf, while R3 and R4 represent the non-melt regions. These profiles are
434 arranged from bottom to top. Melt is observed in the northwest (ice front) and southern parts
435 (grounding line) of the shelf above the Schirmacheroasen, while the central part of the shelf
436 remains mostly unaffected by melting during the majority of the melt seasons. The ice flow
437 velocity data obtained from SAR data processing for both the surface melt and non-melt regions
438 are evaluated in relation to the distance for the maximum and minimum surface melt periods during
439 the austral summers of 2019-2023.



441 **Fig. 9.** The four profiles R1, R2, R3, and R4 of 30-km long drawn over NIS in the melt and non-
442 melt regions (Background image is surface ice flow velocity map estimated during January
443 2023)

444

445 **5.6.1 Profile R1: melt region**

446 Profile R1 in the northwest melt region of NIS was studied during the minimum and
447 maximum Surface Melt Extent (SME) periods from AS 2019-2023 (Figure 21). The ice flow
448 pattern remained consistent, averaging 0.35 m/12 days, during the lowest and highest SME periods
449 in the austral summer of 2021–2022. In contrast, between the lowest and highest SME periods in
450 the austral summer of 2020–2021, the velocity increased by twice as much, from 0.9 m/12 days to
451 1.8 m/12 days on average. However, a decreasing trend in velocity was observed during the
452 minimum and maximum SME periods in the austral summers of 2019–2020 and 2022–2023, with
453 an average velocity of 1.5 m/12 days. Notably, beyond a 10 km distance, the velocity gradually
454 rose, likely due to the declining slope towards the ice front. This 10 km range coincided with an
455 ice rise/rumple feature that provided support to the ice flow.

456 **5.6.2. Profile R2: melt region**

457 Profile R2, located at the grounding line above the Schirmacheroasen in the southern region
458 of NIS (Figure 21), was analyzed and presented in figure 23. Similar velocity patterns were
459 observed in AS 2019–2022, 2020–2021, and 2022–2023, with average and maximum ice flow
460 rates of around 1 m/12 days and 1.4 m/days, respectively. However, AS 2021–2022 showed a
461 significant decrease in velocity compared to previous austral summers, almost half in magnitude.
462 The presence of high ice flow near the grounding line suggests the presence of melt ponds. As the
463 distance increased up to 15 km, ice flow declined, likely due to reduced melting or the absence of
464 water bodies. Beyond 15 km, linear water bodies were observed, indicating reduced ice flow and
465 limited meltwater availability.

466 **5.6.3. Profile R3 & R4: non-melt region**

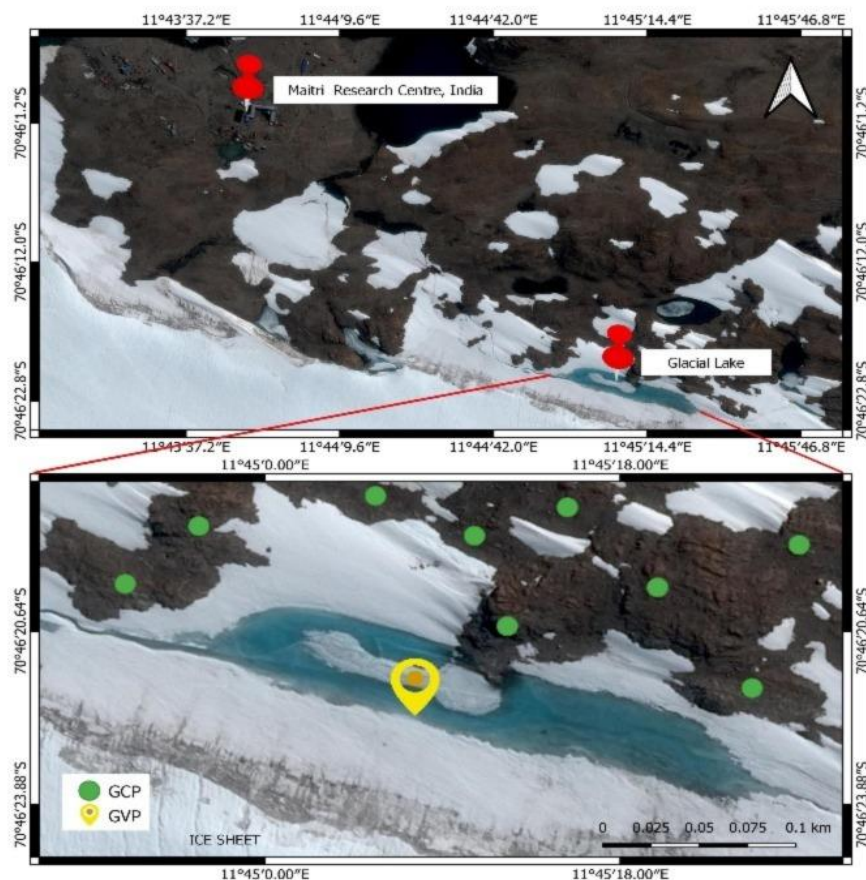
467 In the central part of NIS, specifically above the Schirmacheroasen, non-melt regions R3
468 and R4 were identified. The velocity profiles during the minimum and maximum SME periods of
469 the austral summer of 2019-2023, as depicted in Figure 24, provide insights into the behavior of

470 ice flow in these regions. For both R3 and R4, a consistent pattern of velocity was observed during
471 the austral summer of 2019-2020, with the average and maximum velocities ranging from 0.9m to
472 1 m/12 days and 1.1 to 1.3 m/12 days, respectively, exhibiting negligible variations. This similar
473 velocity pattern persisted during the austral summer of 2020-2021 and 2022-2023, maintaining an
474 average velocity of 1 m/12 days.

475 In the austral summer of 2021-2022, there was a slight increase in maximum velocity (0.4
476 to 0.56 m/12 days), while the average velocity remained constant at 0.3 m/12 days. This suggests
477 a stable flow with minimal variation in maximum velocity. Overall, there was a gradual increase
478 in velocity with distance, indicating a decreasing slope towards the ocean. Notably, in the non-
479 melt regions of R3 and R4, velocity remained relatively constant throughout the examined austral
480 summer periods.

481 **5.7 Field Validation**

482 The fieldwork was conducted during the austral summer period of 2022-2023 as a part of
483 the 42nd Indian scientific expedition to Antarctica. During the fieldwork, a melt pond (figure 25)
484 was considered near the Maitri, Indian research base (due to logistical feasibility) located at
485 (11°45'6.786"E, 70°46'22.475"S) in Dronning Maud Land, East Antarctica for installation of
486 Pressure Sensor Assembly (PSA)(Fausto et al. 2012). Due to the unavailability of cloud-free
487 satellite-based optical data over the selected melt pond, Unmanned Aerial Survey was carried out
488 over the selected melt pond using P4 multispectral sensor. Details about the pressure sensor and
489 UAV sensor used are given in Table 4.



490

491 **Fig. 10.** Validation site: Glacial Lake / melt pond selected near the Maitri, Indian research
 492 station located in Dronning Maud land, East Antarctica.

493

494 **Table 1** Details about the sensor used for field validation i.e., pressure sensor for depth
 495 estimation (equivalent water level) and a multispectral sensor for estimating the depth over the
 496 melt pond using MPD model

497

Instrument type	Manufacturer	Model type	Accuracy
Pressure sensor	KELLER Druckmesstechnik AG, Switzerland	DCX-22 SG	±2.5 (cm)
Multispectral sensor	SZ DJI Technology Co Ltd (DJI), China	P4 Multispectral	Wavelength accuracy of ±1 nm

498

499

500

501

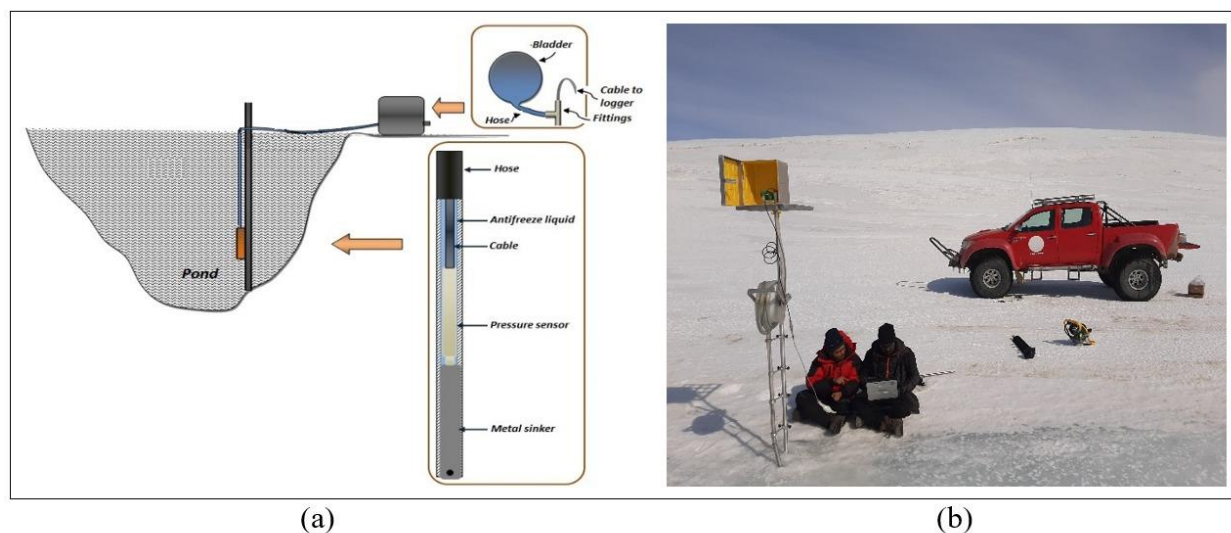
502

503 **5.7.1. UAV with P4 Multispectral sensor:**

504 The P4 RTK (real-time kinematic) Multispectral is a high-precision UAV that is equipped
505 with a multispectral camera as shown in figure 26. This sensor allows the UAV to capture images
506 of the study area in multiple spectral bands. The P4 Multispectral has six 1/2.9-inch CMOS
507 sensors, including one RGB sensor for visible light imaging and five monochrome sensors (Blue
508 (B): 450 nm; Green (G): 560 nm; Red (R): 650 nm; Red edge (RE): 730 nm; Near-infrared (NIR):
509 840 nm) for multispectral imaging. The RGB sensor has an effective pixel count of 2.08 MP, and
510 the five monochrome sensors each have an effective pixel count of 2.08 MP. The P4 Multispectral
511 can be used to collect valuable data about the earth's surface, such as crop health, forest health,
512 and environmental conditions. The present study attempts to showcase the ability of using UAV
513 data for cryosphere studies in Antarctica.

514 **5.7.2. Pressure Sensor Assembly (PSA):**

515 The PSA's current design is given in graphical representation as shown in figure 27. An
516 armored silicon hose of 26mm diameter with a total length of 10m that houses a pressure sensor
517 was used. The pressure sensor is attached to a 23-cm long, slightly larger than 26 mm iron rod that
518 is inserted with silicone sealant and connected with hose clamps in the bottom half of the hose.
519 The rod serves as both a waterproof closure and a dead weight. A T-junction is fitted at the top
520 end of the hose to allow the logger cable exiting the closed PSA system to link the pressure sensor
521 to the logger. The other T-junction branch connects to a 2L expansion rubber bladder. The bladder
522 is generally half-full to enable volume variations in the antifreeze (for example, due to sun heating)
523 without causing pressure buildup in the assembly. The hose is filled with an antifreeze solution
524 (ethylene glycol with water in the proportion 50:50) and the PSA was mounted on a pole of 5-m
525 long erected in the pond/lake area with the help of a Teflon pulley and guides. The pulley
526 arrangement is made to ensure that the pressure sensor slides down as the melting progress and
527 remains in contact with the pond ice floor /bottom bed surface over which meltwater is ponding.



528

529 **Fig. 11.** (a) The graphical representation of the Pressure Sensor Assembly installation over the
 530 melt pond selected for the study (b) The bladder box on the T-junction is fitted at the top end of
 531 the hose to allow the logger cable exiting the closed PSA system and other T-junction's branch
 532 connects to a 2L expansion rubber bladder

533 The setup was installed by drilling up to 3 m into the frozen pond (location) with a Jiffy
 534 ice auger (4G four stroke) and extenders by late November 2022 before melting. The sensor used
 535 is a DCX-22 data logger which is a versatile device designed for measuring water level, water
 536 pressure, and temperature. The Sealed Gauge variant delivers the highest level of accuracy and is
 537 well-suited for submersion applications. With an extended battery life, the DCX-22 data logger
 538 can record data for up to 10 years, capturing measurements at hourly intervals.

539 **5.7.3. PSA data collection:**

540 The pressure sensor was programmed to collect pressure and temperature data for every 15
 541 minutes with the help of the data logger attached to the sensor. Data gaps were encountered when
 542 the sensor was exposed due to refreezing of pond / low water levels post-late December 2022. Data
 543 was retrieved from the data logger on a daily basis to avoid data loss due to low battery/memory
 544 and also to ensure that the sensor bottom is always in contact with the melt pond ice floor/bottom
 545 bed surface. In the present study, the melt pond/SGL depth is defined as the vertical distance
 546 between the water level and the lowest point of the melt pond/SGL bed within the cross-section of
 547 the melt pond/SGL. The mean temperature and pressure from the melt pond bottom as measured
 548 by the sensor during the field period are shown in figure 28.

549 The hydrostatic pressure of a fluid in the bar is measured and stored by the DCX-22 device.
550 The conversion of pressure from bar to water column level in meters of water (mH₂O) is
551 significantly affected by the density of the medium. The KOLIBRI Desktop software (Leitner et
552 al. 2013) utilizes equation (5) to calculate the height of the water column. A water density of
553 999.89 kg/m³ is considered as the average temperature on 20th December 2022 was found to be
554 around 1°C. The iron rod length has been compensated for the depth estimates.

$$555 \quad d = \frac{P}{\rho * g} \quad (5)$$

556 where P = hydrostatic pressure (N/m²), ρ = water density (kg/m³), g = gravitational acceleration
557 (m/s²), d = height of water column (m)

558 **5.7.4. GCPs and GVPs**

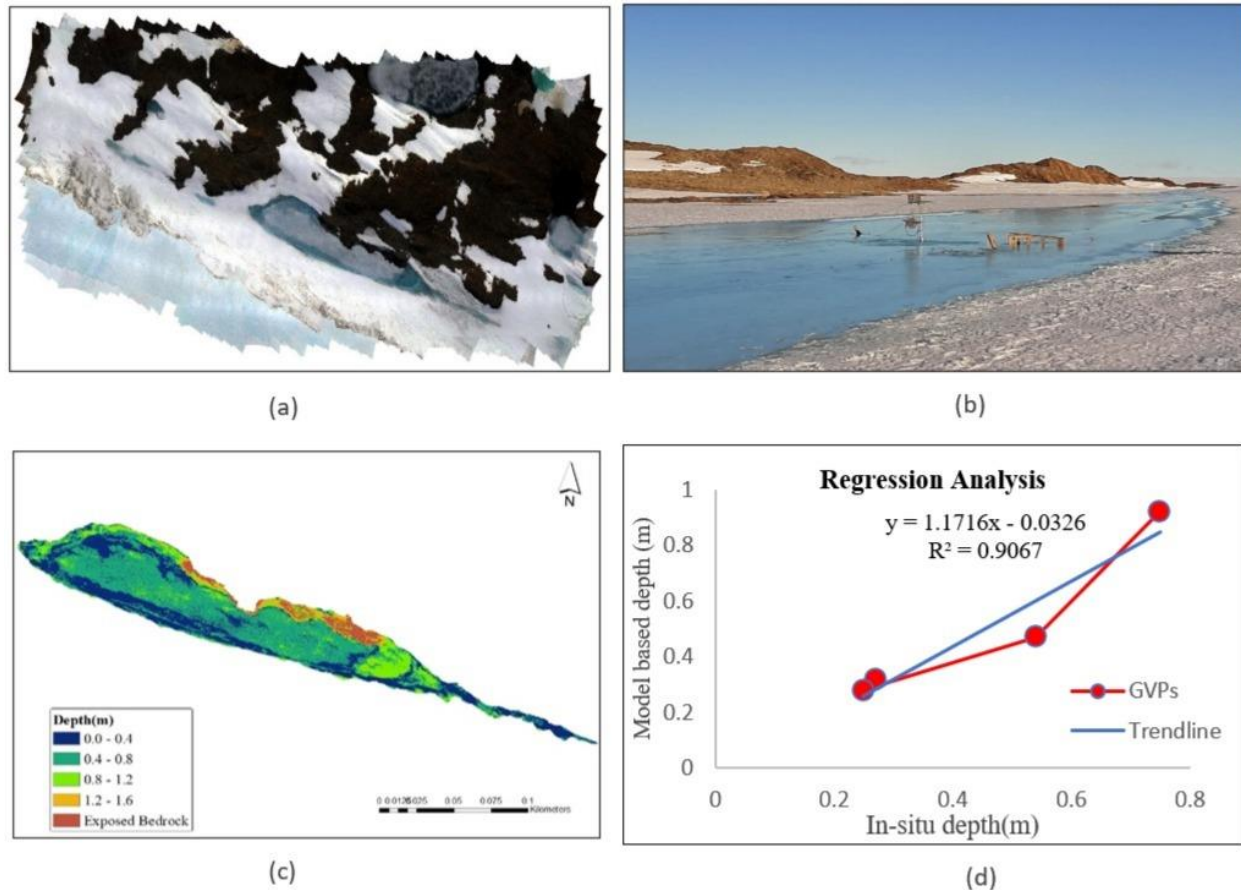
559 The ground control points (GCPs) were established on the field (figure 29) using printed white
560 crosses over the stable regions and the melt pond to achieve high positional accuracies and to
561 minimize elevation-dependent biases. The GCP survey was carried out using SP80 Spectra
562 Precision GNSS receivers. Manual measurements of pond depth were also carried out at different
563 points spread across the pond's periphery. The PSA installation was aimed at depth measurement
564 interior to the melt pond where manual interventions were not feasible as the melt progresses
565 (presence of slush, wide melt channels, etc.). The PSA installed point and manual measurement
566 points were also surveyed as ground validation points (GVPs).

567

568 **5.7.5. Melt pond depth estimation**

569 The radiative transfer model was employed to estimate the depth of the melt pond using multispectral data
570 collected from UAV (Tovar-Sánchez et al. 2021 and Archibold et al. 2015). The estimated depth profile is
571 presented in Figure 30. The model-based results were compared with measurements obtained through PSA
572 and manual measurements. The comparison is summarized in Table 5. Variations in the recorded depths
573 of melt ponds arise from uncertainties and the discrepancy in timing between measurements and aerial
574 surveys conducted at various intervals throughout the observation day. Figure 30 illustrates the
575 regression analysis conducted to compare the field-based depth measurements with the model-based
576 results. The Pearson's correlation coefficient of 0.9 indicates a strong linear positive correlation

577 between the two datasets. The comparison was performed by calculating the root-mean-square error
 578 (RMSE) between the physical in-situ measurements obtained at the field points and the results derived
 579 from the model.



580
 581 **Fig. 12.** (a) An aerial view of the selected melt pond, the RGB image of the lake obtained from P4
 582 multispectral sensor, (b) The view of the lake during the peak melting period, on 20th December
 583 2022, (c) The model-based melt pond depth derived from the UAV survey on 20th December 2022,
 584 (d) Correlation analysis of the measured values

585 **Table 2** Depth values obtained from the pressure sensor and Melt Pond depth model for 20th
 586 December 2022

Parameters	Findings
Date of validation / UAV survey data	20 th December 2022
Model-based depth at GVP	0.75 ± 0.2m
PSA-based depth at GVP	0.92 ± 0.03 m
RMSE at GVP	0.17

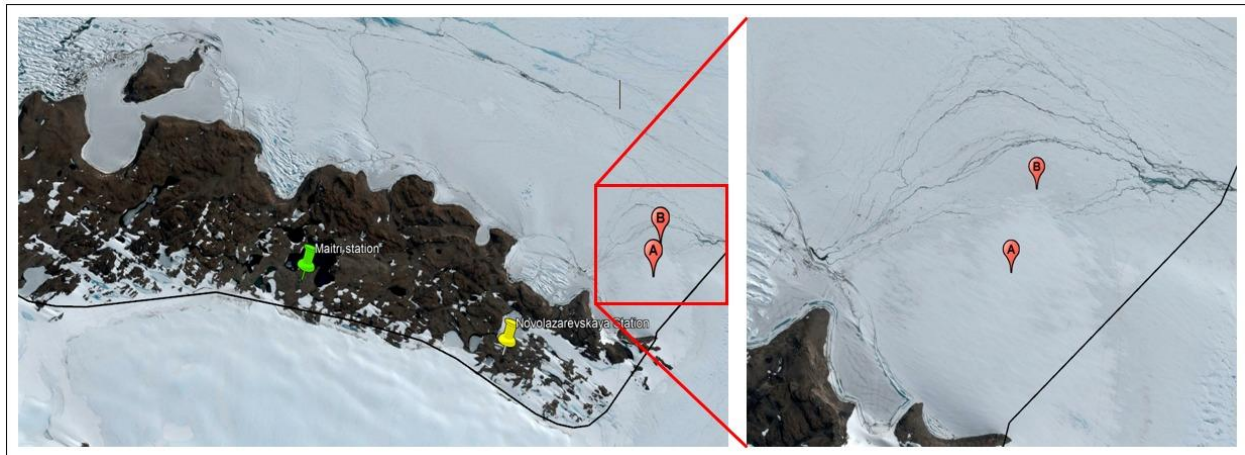
587

588 5.7.6. Limitations

589 The present study analyzed the surface melt NIS which is 130 m wide and 80 m long (Dell
590 et al. 2020) with a large number of melt ponds and SGLs. The parameters studied are highly
591 dynamic and varied in temporal and spatial evolution (Zhu et al. 2023). The depth estimation over
592 NIS was limited only to the spatial extent from 70.3823°S, 10.3667°E to 76.7242°S, 12.8838°E.
593 This study is confined to the surface melt in the form of melt ponds and SGLs during the period
594 from 2000 to 2023. Various factors such as (a) large or small debris slumps, (b) ice calving, (c)
595 katabatic wind effect, (d) pond floor collapse, (e) subaqueous melt, (f) structural collapse and (g)
596 variations in water storage caused by a changing balance between water filling (melting) and
597 drainage (discharge) are not considered in detecting the changes in pond/lake water level. These
598 factors can all contribute to changes in water level, and by analyzing the data, scientists can better
599 understand the causes of these changes and the potential impacts on the environment. Due to
600 logistical constraints, the installation was done at only one melt pond location. The PSA data is
601 used only to validate the model-based melt pond depth estimation in addition to manual depth
602 estimations.

603 5.8 Field-based ice flow motion

604 Due to logistical feasibility, field validation of ice flow was conducted using SP80 Spectra
605 Precision GNSS receivers. Two ground control points (GCPs) were established near the grounding
606 line of the NIS during 29th December 2022 to 10th January 2023, with a 12-day interval (Figure
607 31). This data collection timeframe was synchronized with Sentinel-1 satellite data acquisition.
608 The survey was carried out in static mode, and post-processing of the base-related data was
609 conducted. The obtained displacement values from both the GNSS and DInSAR processes for the
610 NIS are presented in Table 6. It is important to note that uncertainties exist, and discrepancies in
611 the measured displacements are observed due to the different nature of the measurements. The
612 GNSS-based displacement provides a 3D measurement, while the DInSAR-based measurement is
613 in the Line of Sight (LOS) direction (Komac et al. 2015). These differences, along with
614 uncertainties, contribute to the observed variations in the measured displacements (Figure 32).



615

616 **Fig. 13.** Location of two ground control points (GCPs) near the grounding line of the NIS during
617 the period of 29th December 2022 to 10th January 2023, with a 12-day interval.

618 **5.8.1 Uncertainty in surface ice flow velocity**

619 In regions adjacent to the NIS that are considered stable (Schirmacheroasen), a buffer of
620 three pixels (equivalent to approximately 90 m) was applied to compare ice and ice-free zones.
621 Utilizing nearly 200 samples, the Root Mean Square Deviation (RMSD) was found to be
622 approximately 2.8 m/year. It is important to note that the accuracy of these measurements is
623 influenced by the level of coherence observed between the SAR images used. A higher degree of
624 coherence is achieved when employing a smaller temporal resolution and a perpendicular baseline,
625 leading to improved accuracy in the measurements obtained.

626 **6 Conclusion**

627 A comprehensive analysis was conducted on NIS, East Antarctica, focusing on the
628 parameters of supraglacial lakes (SGLs), seasonal surface melt extent, and surface ice flow
629 velocity. Monitoring meltwater is crucial to evaluate the potential destabilization of ice shelves.
630 Relative to the year 2000, the depth, area, and volume of SGLs in NIS have increased. Over the
631 decade from January 2003 to January 2023, the depth and volume of melt ponds grew by a factor
632 of 1.5, while the area increased by a factor of 1.2. While SGL development is limited in the middle
633 of the ice shelf, surface lakes are frequently observed in its interior regions. These cyclic variations
634 in total lake area lead to fluctuations in meltwater volume during the melt season. Limited data
635 enabled the prediction and analysis of seasonal surface melts and surface ice flow velocity
636 fluctuations in NIS, with a focus on the austral summers of 2019–2023. The findings of this study

637 provide essential data for assessing the sensitivity of NIS to climate change and making future
638 projections on sea level rise, particularly regarding surface melting, melt ponds/SGLs, and their
639 impact on ice flow velocity. The impact of meltwater on an ice shelf depends on its quantity,
640 distribution, and the overall state and stability of the ice shelf. With climate change leading to
641 unprecedented polar ice melting, scientists and policymakers are increasingly concerned about the
642 effects of meltwater on ice shelves. It is anticipated that SGL coverage and volume will
643 significantly increase under enhanced atmospheric warming, particularly in ice-shelf regions
644 susceptible to hydro fracture.

645 **Declaration of competing interest**

646

647 The authors declare that they have no known competing financial interests or personal
648 relationships that could have appeared to influence the work reported in this paper.

649

650 **Data availability**

651

652 Data will be made available on request.

653

654 **Acknowledgement**

655 The authors acknowledge the logistical support given by the National Centre for Polar and
656 Ocean Research, Ministry of Earth Sciences, Govt. of India under the Indian Scientific Expedition
657 to Antarctica (ISEA) with project code 42-AMOS/OR-06(2) to undertake this research. The
658 authors gratefully acknowledge the support rendered by PTICL, MM Forgings, TATA STEEL,
659 Jyothy Industries, Rational Technologies and CIIRC, Jyothy Institute of Technology, Bengaluru.

660 **References**

- 661 1. Alimasi N, Enomoto H, Hirasawa N. 2020. Spatiotemporal variation of ice sheet melting
662 in the Antarctic coastal marginal zone and the influence of ice lenses and rain using satellite
663 microwave observation. *Polar Sci* [Internet]. 25(July):100561.
664 <https://doi.org/10.1016/j.polar.2020.100561>
- 665 2. Alley, K. E. Studies of Antarctic Ice Shelf Stability: Surface Melting, Basal Melting, and
666 Ice Flow Dynamics, PhD thesis, Department of Geological Sciences, University of
667 Colorado Boulder, 2017.
- 668 3. Alley KE, Scambos TA, Miller JZ, Long DG, MacFerrin M. 2018. Quantifying
669 vulnerability of Antarctic ice shelves to hydrofracture using microwave scattering

- 670 properties. Remote Sens Environ. 210(January):297–306.
671 <https://doi.org/10.1016/j.rse.2018.03.025>
- 672 4. Aoki, S., Takahashi, T., Yamazaki, K. et al. Warm surface waters increase Antarctic ice
673 shelf melt and delay dense water formation. *Commun Earth Environ* 3, 142 (2022).
674 <https://doi.org/10.1038/s43247-022-00456-z>
- 675 5. Archibold AR, Rahman MM, Yogi Goswami D, Stefanakos EK. 2015. The effects of
676 radiative heat transfer during the melting process of a high temperature phase change
677 material confined in a spherical shell. *Appl Energy*. 138:675–684.
678 <https://doi.org/10.1016/j.apenergy.2014.10.086>
- 679 6. Arthur JF, Stokes C, Jamieson SSR, Carr JR, Leeson AA. 2020. Recent understanding of
680 Antarctic supraglacial lakes using satellite remote sensing. *Prog Phys Geogr*. 44(6):837–
681 869. <https://doi.org/10.1177/0309133320916114>
- 682 7. Arthur JF, Stokes CR, Jamieson SSR, Rachel Carr J, Leeson AA. 2020. Distribution and
683 seasonal evolution of supraglacial lakes on Shackleton Ice Shelf, East Antarctica.
684 *Cryosphere*. 14(11):4103–4120. <https://doi.org/10.5194/tc-14-4103-2020>
- 685 8. Arthur JF, Stokes CR, Jamieson SSR, Rachel Carr J, Leeson AA, Verjans V. 2022. Large
686 interannual variability in supraglacial lakes around East Antarctica. *Nat Commun*. 13(1):1–
687 12. <https://doi.org/10.1038/s41467-022-29385-3>
- 688 9. Banwell AF, Willis IC, Macdonald GJ, Goodsell B, Macayeal DR. Direct measurements of
689 ice-shelf flexure caused by surface meltwater ponding and drainage. *Nat Commun*
690 [Internet].(2019):1–10. <https://doi.org/10.1038/s41467-019-08522-5>
- 691 10. Barella R, Callegari M, Marin C, Klug C, Sailer R, Galos SP, Dinale R, Gianinetto M,
692 Notarnicola C. 2022. Combined Use of Sentinel-1 and Sentinel-2 for Glacier Mapping: An
693 Application over Central East Alps. *IEEE J Sel Top Appl Earth Obs Remote Sens*.
694 15:4824–4834. <https://doi.org/10.1109/JSTARS.2022.3179050>
- 695 11. Baumhoer CA, Dietz AJ, Dech S, Kuenzer C. 2018. Remote Sensing of Antarctic Glacier
696 and Ice-Shelf Front Dynamics — A Review. :1–28. <https://doi.org/10.3390/rs10091445>
- 697 12. Bell RE, Banwell AF, Trusel LD, Kingslake J. 2018. Antarctic surface hydrology and
698 impacts on ice-sheet mass balance. *Nat Clim Chang* [Internet]. 8(12):1044–1052.
699 <https://doi.org/10.1038/s41558-018-0326-3>
- 700 13. Bell RE, Chu W, Kingslake J, Das I, Tedesco M, Tinto KJ, Zappa CJ, Frezzotti M,
701 Boghosian A, Lee WS. 2017. Antarctic ice shelf potentially stabilized by export of

- 702 meltwater in surface river. *Nature* [Internet]. 544(7650):344–348.
703 <https://doi.org/10.1038/nature22048>
- 704 14. Brogioni M, Andrews MJ, Urbini S, Jezek KC, Johnson JT, Leduc-Leballeur M, MacElloni
705 G, Ackley SF, Bringer A, Brucker L, et al. 2023. Ice Sheet and Sea Ice Ultrawideband
706 Microwave radiometric Airborne eXperiment (ISSIUMAX) in Antarctica: first results from
707 Terra Nova Bay. *Cryosphere*. 17(1):255–278. <https://doi.org/10.5194/tc-17-255-2023>
- 708 15. Buzzard SC, Feltham DL, Flocco D. 2018. A Mathematical Model of Melt Lake
709 Development on an Ice Shelf. *J Adv Model Earth Syst*. 10(2):262–283.
710 <https://doi.org/10.1002/2017MS001155>
- 711 16. Cavalieri DJ, Parkinson CL. 2008. Antarctic sea ice variability and trends, 1979–2006. *J*
712 *Geophys Res*. 113(C7):1–19. <https://doi.org/10.1029/2007jc004564>
- 713 17. Colosio P, Tedesco M, Ranzi R, Fettweis X. 2021. Surface melting over the Greenland ice
714 sheet derived from enhanced resolution passive microwave brightness temperatures (1979-
715 2019). *Cryosphere*. 15(6):2623–2646. <https://doi.org/10.5194/tc-15-2623-2021>
- 716 18. Cook AJ, Vaughan DG. 2010. Overview of areal changes of the ice shelves on the Antarctic
717 Peninsula over the past 50 years. *Cryosphere*. 4(1):77–98. [https://doi.org/10.5194/tc-4-77-](https://doi.org/10.5194/tc-4-77-2010)
718 2010
- 719 19. Dell R, Arnold N, Willis I, Banwell A, Williamson A, Pritchard H, Orr A. 2020. Lateral
720 meltwater transfer across an Antarctic ice shelf. *Cryosphere*. 14(7):2313–2330.
721 <https://doi.org/10.5194/tc-14-2313-2020>
- 722 20. Dell RL, Banwell AF, Willis IC, Arnold NS, Halberstadt ARW, Chudley TR, Pritchard HD.
723 2022. Erratum: Supervised classification of slush and ponded water on Antarctic ice
724 shelves using Landsat 8 imagery (*Journal of Glaciology* 68: 268 (401-414) DOI:
725 10.1017/jog.2021.114). *J Glaciol*. 68(268):415–416. <https://doi.org/10.1017/jog.2022.15>
- 726 21. Dirscherl M, Dietz AJ, Kneisel C, Kuenzer C. 2020. Automated mapping of antarctic
727 supraglacial lakes using a machine learning approach. *Remote Sens*. 12(7).
728 <https://doi.org/10.3390/rs12071203>
- 729 22. Fausto RS, Van As D, Ahlstrøm AP, Citterio M. 2012. Instruments and methods: Assessing
730 the accuracy of Greenland ice sheet ice ablation measurements by pressure transducer. *J*
731 *Glaciol*. 58(212):1144–1150. <https://doi.org/10.3189/2012JoG12J075>
- 732 23. Fricker HA, Arndt P, Brunt KM, Datta RT, Fair Z, Jasinski MF, Kingslake J, Magruder LA,
733 Moussavi M, Pope A, et al. 2021. ICESat-2 Meltwater Depth Estimates: Application to

- 734 Surface Melt on Amery Ice Shelf, East Antarctica. *Geophys Res Lett.* 48(8).
735 <https://doi.org/10.1029/2020GL090550>
- 736 24. Friedl P. 2019. Derivation of glaciological parameters from time series of multi-mission
737 remote sensing data - Applications to glaciers in Antarctica and the Karakoram (January).
- 738 25. Furfaro R, Picca P, Kargel JS, Science P. 2014. Global Land Ice Measurements from Space.
739 *Glob L Ice Meas from Sp.*(July). <https://doi.org/10.1007/978-3-540-79818-7>
- 740 26. Gardner AS, Sharp MJ. 2010. A review of snow and ice albedo and the development of a
741 new physically based broadband albedo parameterization. *J Geophys Res Earth Surf.*
742 115(1):1–15. <https://doi.org/10.1029/2009JF001444>
- 743 27. Geetha Priya M, Deva Jefflin AR, Luis AJ, Bahuguna IM. 2022. Estimation of surface melt
744 induced melt pond depths over Amery Ice Shelf, East Antarctica using Multispectral and
745 ICESat-2 data. *Disaster Adv.* 15(8):1–8. <https://doi.org/10.25303/1508da01008>
- 746 28. Ghiz ML, Scott RC, Vogelmann AM, Lenaerts JTM, Lazzara M, Lubin D. 2021. Energetics
747 of surface melt in West Antarctica. *Cryosphere.* 15(7):3459–3494.
748 <https://doi.org/10.5194/tc-15-3459-2021>
- 749 29. Halas P, Mouginot J, de Fleurian B, Langebroek PM. 2023. Impact of seasonal fluctuations
750 of ice velocity on decadal trends observed in Southwest Greenland. *Remote Sens Environ.*
751 285(January). <https://doi.org/10.1016/j.rse.2022.113419>
- 752 30. Hall DK, Nghiem S V., Schaaf CB, DiGirolamo NE, Neumann G. 2009. Evaluation of
753 surface and near-surface melt characteristics on the Greenland ice sheet using MODIS and
754 QuikSCAT data. *J Geophys Res Earth Surf.* 114(4):1–13.
755 <https://doi.org/10.1029/2009JF001287>
- 756 31. Hawes IAN, Safi K, Sorrell B, Webster-brown J, Arscott D. 2011. Summer-winter
757 transitions in Antarctic ponds I : The physical environment Summer – winter transitions in
758 Antarctic ponds I: The physical environment. (May).
759 <https://doi.org/10.1017/S0954102011000046>
- 760 32. Horwath M, Dietrich R, Baessler M, Nixdorf U, Steinhage D, Fritzsche D, Damm V,
761 Reitmayr G. 2006. Nivlisen, an Antarctic ice shelf in Dronning Maud Land: Geodetic-
762 glaciological results from a combined analysis of ice thickness, ice surface height and ice-
763 flow observations. *J Glaciol.* 52(176):17–30.
764 <https://doi.org/10.3189/172756506781828953>
- 765 33. Husman SDR, Hu Z, Wouters B, Munneke PK, Veldhuijsen S, Lhermitte S . 2022. Remote

- 766 Sensing of Surface Melt on Antarctica : Opportunities and Challenges. IEEE J Sel Top Appl
767 Earth Obs Remote Sens. PP(Xxx):1–20vol. 16, pp. 2462-2480, 2023, doi:
768 10.1109/JSTARS.2022.3216953
- 769 34. Izeboud M, Lhermitte S. 2023. Remote Sensing of Environment Damage detection on
770 antarctic ice shelves using the normalised radon transform. Remote Sens Environ
771 [Internet]. 284(November 2022):113359. <https://doi.org/10.1016/j.rse.2022.113359>
- 772 35. Jakobs CL, Reijmer CH, van den Broeke MR, van de Berg WJ, van Wessem JM. 2021.
773 Spatial Variability of the Snowmelt-Albedo Feedback in Antarctica. J Geophys Res Earth
774 Surf. 126(2). <https://doi.org/10.1029/2020JF005696>
- 775 36. Jakobs CL, Reijmer CH, Smeets CJPP, Trusel LD, Van De Berg WJ, Van Den Broeke MR,
776 Van Wessem JM. 2020. A benchmark dataset of in situ Antarctic surface melt rates and
777 energy balance. J Glaciol. 66(256):291–302. <https://doi.org/10.1017/jog.2020.6>
- 778 37. Johnson A, Fahnestock M, Hock R. 2020. Evaluation of passive microwave melt detection
779 methods on Antarctic Peninsula ice shelves using time series of Sentinel-1 SAR. Remote
780 Sens Environ [Internet]. 250(February):112044. <https://doi.org/10.1016/j.rse.2020.112044>
- 781 38. Kaushik S, Cerino B, Trouve E, Karbou F, Yan Y, Ravanel L, Magnin F. 2022. Analysis of
782 the Temporal Evolution of Ice Aprons in the Mont-Blanc Massif Using X and C-Band SAR
783 Images. Front Remote Sens. 3(June):1–17. <https://doi.org/10.3389/frsen.2022.930021>
- 784 39. Kingslake J, Ely JC, Das I, Bell RE. 2017. Letter. Nat Publ Gr [Internet]. 544(7650):349–
785 352. <https://doi.org/10.1038/nature22049>
- 786 40. Komac M, Holley R, Mahapatra P, van der Marel H, Bavec M. 2015. Coupling of
787 GPS/GNSS and radar interferometric data for a 3D surface displacement monitoring of
788 landslides. Landslides. 12(2):241–257. <https://doi.org/10.1007/s10346-014-0482-0>
- 789 41. König M, Oppelt N. 2020. A linear model to derive melt pond depth on Arctic sea ice from
790 hyperspectral data. Cryosphere. 14(8):2567–2579. [https://doi.org/10.5194/tc-14-2567-](https://doi.org/10.5194/tc-14-2567-2020)
791 2020
- 792 42. Konovalov Y V. 2021. Abatement of Ocean-Wave Impact by Crevasses in an Ice Shelf
793 Abatement of Ocean-Wave Impact by Crevasses in an Ice Shelf. (January).
794 <https://doi.org/10.3390/jmse9010046>
- 795 43. Lampkin DJ, Karmoskay CC. 2009. Surface melt magnitude retrieval over Ross Ice Shelf,
796 Antarctica using coupled MODIS near-IR and thermal satellite measurements. Cryosph
797 Discuss. 3(3):1069–1107. <https://doi.org/10.5194/tcd-3-1069-2009>

- 798 44. Mahagaonkar, A., Moholdt, G., and Schuler, T. V.: Recent Evolution of Supraglacial Lakes
799 on ice shelves in Dronning Maud Land, East Antarctica, *The Cryosphere Discuss.*
800 [preprint], <https://doi.org/10.5194/tc-2023-4>, in review, 2023.
- 801 45. Leitner JF, Perteneder F, Liu C, Rendl C, Haller M. 2013. Kolibri - Tiny and fast gestures
802 for large pen-based surfaces. *Conf Hum Factors Comput Syst - Proc.*:1789–1798.
803 <https://doi.org/10.1145/2470654.2466236>
- 804 46. Leppäranta M, Luttinen A, Arvola L. 2020. Physics and geochemistry of lakes in Vestfjella,
805 Dronning Maud Land. *Antarct Sci.* 32(1):29–42.
806 <https://doi.org/10.1017/S0954102019000555>
- 807 47. Liang D, Guo H, Zhang L, Cheng Y, Zhu Q, Liu X. 2021. Time-series snowmelt detection
808 over the Antarctic using Sentinel-1 SAR images on Google Earth Engine. *Remote Sens*
809 *Environ.* 256(February). <https://doi.org/10.1016/j.rse.2021.112318>
- 810 48. Lindbäck K, Moholdt G, Nicholls KW, Hattermann T, Pratap B, Thamban M, Matsuoka K.
811 2019. Spatial and temporal variations in basal melting at Nivlisen ice shelf, East Antarctica,
812 derived from phase-sensitive radars. *Cryosphere.* 13(10):2579–2595.
813 <https://doi.org/10.5194/tc-13-2579-2019>
- 814 49. Liu C, Hu R, Wang Y, Lin H, Zeng H, Wu D, Liu Z, Dai Y, Song X, Shao C. 2022.
815 Monitoring water level and volume changes of lakes and reservoirs in the Yellow River
816 Basin using ICESat-2 laser altimetry and Google Earth Engine. *J Hydro-Environment Res*
817 [Internet]. 44(May):53–64. <https://doi.org/10.1016/j.jher.2022.07.005>
- 818 50. Liu H, Wang L, Jezek KC. 2006. Spatiotemporal variations of snowmelt in Antarctica
819 derived from satellite scanning multichannel microwave radiometer and Special Sensor
820 Microwave Imager data (1978-2004). *J Geophys Res Earth Surf.* 111(1).
821 <https://doi.org/10.1029/2005JF000318>
- 822 51. Lombardi D, Gorodetskaya I, Barruol G, Camelbeeck T. 2019. Thermally induced
823 icequakes detected on blue ice areas of the East Antarctic ice sheet. *Ann Glaciol.*
824 60(79):45–56. <https://doi.org/10.1017/aog.2019.26>
- 825 52. Luis AJ, Alam M, Jawak SD. 2022. Spatiotemporal change analysis for snowmelt over the
826 Antarctic ice shelves using scatterometers. (November):1–18.
827 <https://doi.org/10.3389/frsen.2022.953733>
- 828 53. Lund J, Forster RR, Deeb EJ, Liston GE, Skiles SMK, Marshall HP. 2022. Interpreting
829 Sentinel-1 SAR Backscatter Signals of Snowpack Surface Melt/Freeze, Warming, and

- 830 Ripening, through Field Measurements and Physically-Based SnowModel. *Remote Sens.*
831 14(16). <https://doi.org/10.3390/rs14164002>
- 832 54. Manickam S, Bhattacharya A, Singh G, Yamaguchi Y. 2017. Estimation of Snow Surface
833 Dielectric Constant from Polarimetric SAR Data. *IEEE J Sel Top Appl Earth Obs Remote*
834 *Sens.* 10(1):211–218. <https://doi.org/10.1109/JSTARS.2016.2588531>
- 835 55. Masek JG, Wulder MA, Markham B, McCorkel J, Crawford CJ, Storey J, Jenstrom DT.
836 2020. Landsat 9: Empowering open science and applications through continuity. *Remote*
837 *Sens Environ.* 248(October 2020). <https://doi.org/10.1016/j.rse.2020.111968>
- 838 56. Mortimer CA, Sharp M, Wouters B. 2016. Glacier surface temperatures in the Canadian
839 High Arctic, 2000-15. *J Glaciol.* 62(235):963–975. <https://doi.org/10.1017/jog.2016.80>
- 840 57. Moussavi M, Pope A, Halberstadt ARW, Trusel LD, Cioffi L, Abdalat W. 2020. Antarctic
841 supraglacial lake detection using landsat 8 and sentinel-2 imagery: Towards continental
842 generation of lake volumes. *Remote Sens.* 12(1). <https://doi.org/10.3390/RS12010134>
- 843 58. Orr A, Deb P, Clem KR, Gilbert E, Bromwich DH, Boberg F, Colwell S, Hansen N, Lazzara
844 MA, Mooney PA, et al. 2022. Characteristics of surface “melt potential” over Antarctic ice
845 shelves based on regional atmospheric model simulations of summer air temperature
846 extremes from 1979/80 to 2018/19. *J Clim.*:1–61. <https://doi.org/10.1175/jcli-d-22-0386.1>
- 847 59. Oza SR, Singh RKK, Vyas NK, Sarkar A. 2011. Study of inter-annual variations in surface
848 melting over Amery Ice Shelf, East Antarctica, using space-borne scatterometer data. *J*
849 *Earth Syst Sci.* 120(2):329–336. <https://doi.org/10.1007/s12040-011-0055-8>
- 850 60. Valerio L P, Shaw J, Gonzalez F, Robinson S, Kate J H. 2022. Contemporary Remote
851 Sensing Tools for Integrated Assessment and Conservation Planning of Ice-free Antarctica.
852 (June):1–22.
- 853 61. Philpot WD. 1989. Bathymetric mapping with passive multispectral imagery. *Appl Opt.*
854 28(8):1569. <https://doi.org/10.1364/ao.28.001569>
- 855 62. Pina P, Vieira G. 2022. UAVs for Science in Antarctica. *Remote Sens.* 14(7):1–39.
856 <https://doi.org/10.3390/rs14071610>
- 857 63. Pope A, Scambos TA, Moussavi M, Tedesco M, Willis M, Shean D, Grigsby S. 2016.
858 Estimating supraglacial lake depth in West Greenland using Landsat 8 and comparison with
859 other multispectral methods. *Cryosphere.* 10(1):15–27. [https://doi.org/10.5194/tc-10-15-](https://doi.org/10.5194/tc-10-15-2016)
860 2016
- 861 64. Qiao G, Yuan X, Florinsky I, Popov S, He Y, Li H. 2023. Topography reconstruction and

- 862 evolution analysis of outlet glacier using data from unmanned aerial vehicles in Antarctica.
863 Int J Appl Earth Obs Geoinf [Internet]. 117(August 2022):103186.
864 <https://doi.org/10.1016/j.jag.2023.103186>
- 865 65. Rakshita C, Sowjanya A, Swathi P, Geetha Priya M. 2023. Velocity Estimation of East
866 Antarctic Glacier with SAR Offset Tracking---An Application of Image Processing. In:
867 Smys S, Tavares JMRS, Shi F, editors. Comput Vis Bio-Inspired Comput. Singapore:
868 Springer Nature Singapore; p. 323–331.
- 869 66. Rintoul SR. 2018. The global influence of localized dynamics in the Southern Ocean.
870 Nature. 558(7709):209–218. <https://doi.org/10.1038/s41586-018-0182-3>
- 871 67. Safa F, Flouzat G. 1989. Speckle removal on radar imagery based on mathematical
872 morphology. Signal Processing. 16(4):319–333. [https://doi.org/10.1016/0165-](https://doi.org/10.1016/0165-1684(89)90029-7)
873 [1684\(89\)90029-7](https://doi.org/10.1016/0165-1684(89)90029-7)
- 874 68. Saunderson D, MacKintosh A, McCormack F, Jones RS, Picard G. 2022. Surface melt on
875 the Shackleton Ice Shelf, East Antarctica (2003-2021). Cryosphere. 16(10):4553–4569.
876 <https://doi.org/10.5194/tc-16-4553-2022>
- 877 69. Sergienko O V. 2022. No general stability conditions for marine ice-sheet grounding lines
878 in the presence of feedbacks. Nat Commun. 13(1). [https://doi.org/10.1038/s41467-022-](https://doi.org/10.1038/s41467-022-29892-3)
879 [29892-3](https://doi.org/10.1038/s41467-022-29892-3)
- 880 70. Sivalingam S, Murugesan GP, Dhulipala K, Kulkarni AV, Devaraj S. 2022. Temporal
881 fluctuations of siachen glacier velocity: a repeat pass sar interferometry based approach.
882 Geocarto Int. 37(17):4888–4910. <https://doi.org/10.1080/10106049.2021.1899306>
- 883 71. Sneed WA, Hamilton GS. 2007. Evolution of melt pond volume on the surface of the
884 Greenland Ice Sheet. Geophys Res Lett. 34(3):4–7.
885 <https://doi.org/10.1029/2006GL028697>
- 886 72. Steiner N, Tedesco M. 2014. A wavelet melt detection algorithm applied to enhanced-
887 resolution scatterometer data over Antarctica (2000-2009). Cryosphere. 8(1):25–40.
888 <https://doi.org/10.5194/tc-8-25-2014>
- 889 73. Stevens LA, Behn MD, McGuire JJ, Das SB, Joughin I, Herring T, Shean DE, King MA.
890 2015. Greenland supraglacial lake drainages triggered by hydrologically induced basal slip.
891 Nature. 522(7554):73–76. <https://doi.org/10.1038/nature14480>
- 892 74. Tovar-Sánchez A, Román A, Roque-Atienza D, Navarro G. 2021. Applications of
893 unmanned aerial vehicles in Antarctic environmental research. Sci Rep [Internet]. 11(1):1–

- 894 8. <https://doi.org/10.1038/s41598-021-01228-z>
- 895 75. Trusel LD, Frey KE, Das SB. 2012. Antarctic surface melting dynamics: Enhanced
896 perspectives from radar scatterometer data. *J Geophys Res Earth Surf.* 117(2).
897 <https://doi.org/10.1029/2011JF002126>
- 898 76. Trusel LD, Pan Z, Moussavi M. 2022. Repeated Tidally Induced Hydrofracture of a
899 Supraglacial Lake at the Amery Ice Shelf Grounding Zone. *Geophys Res Lett.* 49(7):1–11.
900 <https://doi.org/10.1029/2021GL095661>
- 901 77. Tuckett PA, Ely JC, Sole AJ, Lea JM, Livingstone SJ, Jones JM, Van Wessem JM. 2021.
902 Automated mapping of the seasonal evolution of surface meltwater and its links to climate
903 on the Amery Ice Shelf, Antarctica. *Cryosphere.* 15(12):5785–5804.
904 <https://doi.org/10.5194/tc-15-5785-2021>
- 905 78. Tuckett PA, Ely JC, Sole AJ, Livingstone SJ, Davison BJ, Melchior van Wessem J, Howard
906 J. 2019. Rapid accelerations of Antarctic Peninsula outlet glaciers driven by surface melt.
907 *Nat Commun [Internet].* 10(1). <https://doi.org/10.1038/s41467-019-12039-2>
- 908 79. Vaňková I, Cook S, Winberry JP, Nicholls KW, Galton-Fenzi BK. 2021. Deriving Melt
909 Rates at a Complex Ice Shelf Base Using In Situ Radar: Application to Totten Ice Shelf.
910 *Geophys Res Lett.* 48(7). <https://doi.org/10.1029/2021GL092692>
- 911 80. Yuan X, Qiao G, Li Y, Li H, Xu R. 2020. Modelling of glacier and ice sheet micro-
912 topography based on unmanned aerial vehicle data, Antarctica. *Int Arch Photogramm*
913 *Remote Sens Spat Inf Sci - ISPRS Arch.* 43(B3):919–923. [https://doi.org/10.5194/isprs-](https://doi.org/10.5194/isprs-archives-XLIII-B3-2020-919-2020)
914 [archives-XLIII-B3-2020-919-2020](https://doi.org/10.5194/isprs-archives-XLIII-B3-2020-919-2020)
- 915 81. Zhu J, Tan S, Tsang L, Kang DH, Kim E. 2021. Snow Water Equivalent Retrieval Using
916 Active and Passive Microwave Observations. *Water Resour Res.* 57(7):1–21.
917 <https://doi.org/10.1029/2020WR027563>
- 918 82. Zhu Q, Guo H, Zhang L, Liang D, Liu X, Zhou H. 2023. High-resolution spatio-temporal
919 analysis of snowmelt over Antarctic Peninsula ice shelves from 2015 to 2021 using SAR
920 images High-resolution spatio-temporal analysis of snowmelt over Antarctic Peninsula ice
921 shelves from 2015 to 2021 using SAR images. (March).
922 <https://doi.org/10.1080/17538947.2023.2181991>